Remote Sensing of Environment 249 (2020) 112027

Contents lists available at ScienceDirect

Remote Sensing of Environment

journal homepage: www.elsevier.com/locate/rse

New insights into SMOS sea surface salinity retrievals in the Arctic Ocean

Alexandre Supply[a,*], Jacqueline Boutin[a], Jean-Luc Vergely[b], Nicolas Kolodziejczyk[c], Gilles Reverdin[a], Nicolas Reul[c], Anastasiia Tarasenko[c,d]

[a] Laboratoire d'océanographie et du climat : expérimentations et approches numériques - Institut Pierre Simon Laplace (LOCEAN-IPSL), Sorbonne Université-CNRS-IRD-MNHN, Paris, France
[b] ACRI-St, Guyancourt, France
[c] Laboratoire d'Océanographie Physique et Spatiale (LOPS), Univ. Brest, CNRS, Ifremer, IRD, Brest, France
[d] Arctic and Antarctic Research Institute, Saint-Petersburg, Russia

ARTICLE INFO

Keywords:
SMOS
Sea surface salinity
Arctic Ocean

ABSTRACT

Since 2010, the Soil Moisture and Ocean Salinity (SMOS) satellite mission monitors the earth emission at L-Band. It provides the longest time series of Sea Surface Salinity (SSS) from space over the global ocean. However, the SSS retrieval at high latitudes is a challenge because of the low sensitivity L-Band radiometric measurements to SSS in cold waters and to the contamination of SMOS measurements by the vicinity of continents, of sea ice and of Radio Frequency Interferences. In this paper, we assess the quality of weekly SSS fields derived from swath-ordered instantaneous SMOS SSS (so called Level 2) distributed by the European Space Agency. These products are filtered according to new criteria. We use the pseudo-dielectric constant retrieved from SMOS brightness temperatures to filter SSS pixels polluted by sea ice. We identify that the dielectric constant model and the sea surface temperature auxiliary parameter used as prior information in the SMOS SSS retrieval induce significant systematic errors at low temperatures. We propose a novel empirical correction to mitigate those sources of errors at high latitudes.

Comparisons with in-situ measurements ranging from 1 to 11 m depths spotlight huge vertical stratification in fresh regions. This emphasizes the need to consider in-situ salinity as close as possible to the sea surface when validating L-band radiometric SSS which are representative of the first top centimeter.

SSS Standard deviation of differences (STDD) between weekly SMOS SSS and in-situ near surface salinity significantly decrease after applying the SSS correction, from 1.46 pss to 1.28 pss. The correlation between new SMOS SSS and in-situ near surface salinity reaches 0.94. SMOS estimates better capture SSS variability in the Arctic Ocean in comparison to TOPAZ reanalysis (STDD between TOPAZ and in-situ SSS = 1.86 pss), particularly in river plumes with very large SSS spatial gradients.

1. Introduction

In the context of global warming, Arctic is experiencing an increase of temperature two to three times higher than the global mean average (IPCC, 2018). The freshwater cycle in that region is profoundly modified. The salinity is decreasing (see a review in Carmack et al., 2016) except in the Barents Sea where both temperature and salinity are increasing under the effect of 'Atlantification', i.e. increase of salty supply from North Atlantic waters (Lind et al., 2018). Eventually, in the Arctic Ocean, salinity is the key dynamical variable, ensuring the stability of the water column and controlling the ocean circulation (Carmack, 2007).

The high variability of freshwater inputs is a dominant feature of the Arctic Ocean and induces a large variability in salinity (Carmack et al., 2016; Haine et al., 2015). In addition to the seasonal freshwater input from ice melting, the Arctic Ocean sea surface salinity (SSS) is mainly controlled by numerous river inputs. The Arctic Ocean covers only 1.2% of the global ocean but collects 11% of the freshwater from global river plumes (Shiklomanov et al., 1998) mainly in the interior shelves of the Kara, Laptev and East-Siberian Seas. In addition, the surface water entering poleward through Bering Strait is rather fresh in comparison with salty waters from Atlantic. The third major net source of freshwater in the Arctic Ocean comes from air-sea exchange (precipitation minus evaporation). Freshwater is exported equatorward from the Arctic Ocean at Fram Strait, over the east Greenland shelves, as well as through Davis Strait after crossing Baffin Bay.

* Corresponding author.
E-mail address: alexandre.supply@locean.upmc.fr (A. Supply).

https://doi.org/10.1016/j.rse.2020.112027
Received 13 November 2019; Received in revised form 29 June 2020; Accepted 30 July 2020
Available online 12 August 2020

Since 2010, L-Band radiometer satellite missions (SMOS (2010-present), Kerr et al., 2010, Font et al., 2010), Aquarius (2011–2015, Lagerloef et al., 2008) and SMAP (2015-present, Piepmeier et al., 2017) have demonstrated their abilities to monitor salinity variability at various temporal and spatial scales in synergy with in-situ measurements as reviewed by Vinogradova et al. (2019) and Reul et al. (2020). L-Band radiometry is of particular interest in the Arctic Ocean as it combines the ability to retrieve thin sea ice thickness and salinity. SMOS is the first satellite mission carrying an L-band radiometer (the MIRAS interferometer) allowing to retrieve SSS with an unprecedented temporal coverage. It follows a sun-synchronous circular orbit.

L-Band radiometer measurements are significantly less sensitive to SSS in cold water than in warm tropical conditions (Meissner et al., 2016). However, a very large range of SSS is observed in the Arctic, with salinity close to 0pss in river plumes and reaching 35 pss in the Atlantic water (Carmack et al., 2015). For this reason, L-Band radiometry remains valuable for the detection of large SSS variability and the monitoring of oceanic fronts in the Arctic Ocean (Brucker et al., 2014; Matsuoka et al., 2016; Olmedo et al., 2018; Tang et al., 2018; Tarasenko et al., 2019).

Brucker et al. (2014) and Tang et al. (2018) presented capabilities (monitoring of the river plumes and of upper layer freshwater exchanges between different Arctic Seas and sub-Arctic Oceans) and limits (sea-ice presence) of L-Band SSS retrievals based on Aquarius and SMAP measurements respectively. Köhler et al. (2015) found sea surface temperature (SST) - related bias (−1.2 pss) of SMOS SSS retrieved in cold waters and pollution due to Radio Frequency Interference (RFI) in the northern North Atlantic. Matsuoka et al. (2016) used SMOS SSS monitoring together with ocean colour remote sensing in order to detect the origin (river or ice melting) of salinity interannual anomalies close to the Mackenzie river mouth. Tarasenko et al. (2019) showed the atmospheric influence on the river plume variability in the Laptev Sea at intra-seasonal time scale (a few weeks) based on SMOS SSS. Recently, an SSS retrieval methodology alternative to the one in place in the ESA L2 chain has been proposed with new systematic bias corrections and filtering adjusted to the Arctic Ocean conditions (Olmedo et al., 2018).

Using an accurate SST is critical in order to retrieve SSS with a minimum uncertainty. For instance, at SST = 5 °C and SSS = 35 pss, an error of 1 °C roughly leads to an error of 0.1 K in brightness temperature (TB), which translates into in error of 0.3 pss in the retrieved SSS (Yueh et al., 2001). According to Stroh et al. (2015) and Høyer et al. (2012), systematic differences of various space-based SST measurements in the Arctic Ocean, estimated by comparisons with buoys and ship-based measurements, range from 0.3 to 0.5 °C depending on the season and on the sensor. The temporal and spatial resolution of the SST fields obtained by different optimal analyses vary significantly. This results in significant differences in the estimated SST over highly dynamical and variable regions such as river plumes. A satellite SSS bias related to SST may also be due to flaws in the dielectric constant model that links TB to SSS and SST (Dinnat et al., 2019). The presence of badly detected sea ice can also lead to negative bias on the retrieved SSS (Tang et al., 2018).

The satellite SSS validation is made difficult because of the strong vertical haline stratification observed in the upper Arctic Ocean waters, as L-band radiometer only senses the top centimeter of the ocean (Boutin et al., 2016) and most in-situ sensors probe salinity much deeper (meters). This stratification varies geographically and temporally. The depth of the mixed layer (ML) may be shallower than 10 m in summer in some regions such as the Beaufort Sea (Peralta-Ferriz and Woodgate, 2015).

This paper focuses on validating weekly fields derived from the European Space Agency (ESA) SMOS level 2 (L2) SSS, analyzing potential sources of errors and proposing improvements. A description of the data and methods is first given (section 2 and 3). The influence of stratification on the SSS validation is then investigated (section 4). A first correction of SSS is derived using the pseudo dielectric constant parameter retrieved by the SMOS ESA L2 processing (Waldteufel et al., 2004). The influence of the prior SST on SSS retrieval is further analyzed (section 5). Finally, corrected SMOS weekly SSS are compared against surface salinity from TOPAZ reanalysis and in situ measurements from vessels transect to assess the product content from short to interannual time scales (section 6).

2. Data

2.1. Satellite related parameters

2.1.1. SST

In the SMOS L2 SSS processor, SST provided by European Centre for Medium-Range Weather Forecasts (ECMWF) Integrated Forecasting System (SST_{ECMWF}) are used as priors in the SSS retrievals. These forecasts are initialized 6 to 12 h before by OSTIA SST (Donlon et al., 2012; ECMWF, 2016). The OSTIA SST analysis is generated using a multiscale interpolation of various satellite SST (infrared and microwave SST) and in-situ measurements at a grid spacing close to 5 km.

In this paper, we compare SST_{ECMWF} with the 9 km grid resolution infrared and microwave OI SST produced by REMSS (SST_{REMSS}) that relies on an optimal interpolation of infrared and microwave measurements, but no in-situ measurements (http://www.remss.com/measurements/sea-surface-temperature/oisst-description/). The influence of the SST differences onto the retrieved SSS is estimated as described in section 5.3.

2.1.2. SMOS L2 SSS and Acard

We use the SMOS L2 SSS (uncorrected for Land Sea Contamination) v662 distributed by ESA from 2011 to 2017 in the region bounded by latitude 60°N and 90°N. These products are organized in ½ orbits of instantaneous SSS retrievals. The principle of the ESA L2 SMOS SSS retrieval is recalled in (Boutin et al., 2018; section 3.1 and documents cited herein). SSS are oversampled over an Icosahedral Snyder Equal Area (ISEA) grid at 15 km resolution but the mean spatial resolution of ESA L2 SMOS SSS is close to 50 km. The dielectric constant model of sea water used in the SMOS processor is the Klein and Swift (1977) model (hereafter KS).

We also use the pseudo dielectric constant (Acard) parameter. Acard is an effective L-band dielectric constant retrieved from ~hundreds SMOS multi-angular TB, independent of any SSS or dielectric constant model assumption. It was designed to integrate all available information about surface dielectric characteristics (Waldteufel et al., 2004). Acard allows to synthesize in one parameter the information on the dielectric constant that is contained in all SMOS TB. Since the noise on individual TB is large ($2-3K$), Acard synthesis allows a more precise filtering than a filtering applied on each individual TB. SMOS SSS and Acard are retrieved using a Bayesian approach through the minimization of the χ^2 cost function:

$$\chi^2 = \Sigma_{n=1}^{N} \frac{[Tb_n^{meas} - Tb_n^{mod}(\theta_n, P_i...)]^2}{\sigma_{Tbn}^2} + \Sigma_{n=1}^{M} \frac{[P_i - P_{i0}]^2}{\sigma_{Pi0}^2} \quad (1)$$

where N is the number of measurements available for retrievals in vertical and horizontal polarizations at different incidence angles θ_n, P_i are prior parameters, Tb^{meas} are measured TB corrected for some phenomena, Tb^{mod} are modeled TB. These various components are described for each retrieval in Table 1. Retrievals are initialized with European Centre for Medium-Range Weather Forecasts (ECMWF) (wind speed (WS_{ECMWF}), SST (SST_{ECMWF})). In case of SSS retrieval, both wind speed (WS_{L2}) and SST (SST_{L2}) are retrieved together with SMOS SSS (SSS_{L2}). In case of Acard retrieval ($Acard_{L2}$) only SST (SST_{ACARD}) is retrieved together with Acard. A detailed description of the Acard retrieval in the L2 Ocean Salinity processor is given in appendix-A.

Acard as simulated with KS sea water dielectric constant and ice dielectric constant reported in (Ulaby et al., 1990), varies from

Table 1
Summary of SMOS SSS and Acard retrieval principle in the SMOS L2OS processor.

	SSS retrieval	Acard retrieval
Modeled TBs	Dielectric constant, wind, galactic, atmospheric model components	Flat sea emission
Measured TBs	SMOS multi-angular TBs	SMOS multi-angular TBs corrected from wind, galactic and atmospheric model components
Prior variables	WS_{ECMWF}, SST_{ECMWF}	SST_{ECMWF}
Retrieved variables	SSS_{L2}, WS_{L2}, SST_{L2}	$Acard_{L2}$, SST_{Acard}

approximately 50 in pixels totally covered with sea water to a value close to 0 in pixels totally covered by ice. Hence, pixels partially covered by sea ice exhibit lower Acard values than pure water pixels.

2.1.3. Pre-processed SMOS L3 maps

Level 3 (L3) 7-day moving averages of SMOS ESA L2 parameters are produced each day. The 15-km ISEA grid is kept from L2 to L3, in order to avoid spatial smoothing. Only pixels further than 40 km from land are considered. Each SSS or Acard entering the 7-day average is weighted by a Gaussian weight function with a 3-day standard deviation and by the L2 uncertainty taken as the L2 SSS theoretical error multiplied by the χ^2 value (L2 SSS error and χ^2 estimates are described in Boutin et al., 2018). Level 2 products' flags raised for strong sunglint ('Dg_sun_glint_fov'), moonglint ('Dg_moonglint'), or galactic glints ('Dg_galactic_Noise_Error') are filtered out. L2 measurements for which WS_{ECMWF} is lower than 3 $m.s^{-1}$ or greater than 12 $m.s^{-1}$ are not considered due to larger uncertainties with the roughness model for these ranges of wind speed. L3 SSS uncertainty is estimated through an error propagation of L2 SSS uncertainty estimates.

Frequent revisit of polar areas by SMOS allows typically between 0 and 50 L2 retrievals in each pixel within 7 days. We remove L3 pixels with less than five L2 retrievals and with an average distance to the center of the SMOS track higher than 200 km in order to minimize the influence of uncertain measurements at the edge of the swath. We name SSS_{SMOS} the SMOS SSS obtained after this processing.

2.2. Model reanalysis

We use ARCTIC_REANALYSIS_PHYS_002_003 distributed by the Copernicus Marine Environment Monitoring Service (CMEMS). This product is based on the TOPAZ system in its version 4 (Sakov et al., 2012) that uses the HYCOM model (Chassignet et al., 2009). The TOPAZ reanalysis ingests various in-situ and satellite measurements in order to provide fields of temperature, salinity, sea ice drift or sea ice concentration. Salinity measured by Argo floats and some research cruises are assimilated. TOPAZ does not assimilate SMOS SSS.

The initialization of the model is performed in 1973 with a combination of World Ocean Atlas climatology (WOA05) and Polar Science Center Hydrographic Climatology (PHC version 3.0). In addition to the initialization, a climatology of river runoff is used in order to resolve remaining inaccuracies in evaporation and run-off (CMEMS Arctic Ocean Physical Reanalysis Product User Manual). The river discharge monthly climatology is derived using the Total Runoff Integrating Pathways (TRIP, Oki and Sud., 1998) and run-offs estimates from ERA-interim. SMOS SSS are compared with TOPAZ surface salinity simulated at 0 m depth (SSS_{TOPAZ}). We also used Sea Ice Concentration (SIC) from TOPAZ reanalysis in order to study the influence of sea ice on SMOS SSS.

2.3. In-situ measurements

Satellite L3 parameters are collocated with in situ measurements described below using a nearest neighbor criteria.

2.3.1. Argo profilers

Salinity and temperature from Argo profiling floats are taken from the Coriolis GDAC (Global Data Argo Center, http://www.coriolis.eu.org/). Only measurements flagged as good (flag 1), between 1 and 10 m depth are used.

Argo floats are mainly located in the North Atlantic Ocean between 60°W and 20°E (Fig. 1A), with a few floats in the Chukchi Sea. This spatial distribution results in a very peaky salinity distribution, with a salinity mode close to 35 pss and very few salinities below 34pss (Fig. 1D).

2.3.2. CTD profiles

A large part of the CTD profiles is downloaded from the Coriolis data center. We also consider CTD profiles:

- from two NABOS cruises, in 2013 (Ivanov et al., 2013) and 2015 (Polyakov et al., 2015), in the Kara Sea, Laptev Sea and East-Siberian Sea;
- from the Arctic Floating University collected in 2012 (Makhotin and Ivanov, 2018a,b,c), 2013 and 2014 in the Barents Sea,
- collected in the Laptev Sea and East-Siberian Sea during Swerus C-3 cruise (Björk, 2017);
- in the Beaufort Sea from the Beaufort Gyre Exploration Project website (https://www.whoi.edu/website/beaufortgyre/home).

Only measurements between 1 and 10 m are considered. We noticed a few CTD erroneous measurements. In order to ensure that suspicious measurements are not considered in the validation, we apply a 3σ-filtering with respect to SSS_{TOPAZ} (see section 2.3; only in-situ measurements with an absolute difference between $S_{in\text{-}situ}$ and SSS_{TOPAZ} lower than 3σ (5.85pss) are kept).

CTD casts in the Arctic Ocean cover a larger range of temperature and salinity than Argo (Fig. 1B, D). Indeed, the CTD dataset samples very low salinity areas in the Arctic Ocean in the Beaufort gyre or river plumes, as for example in the Laptev Sea or East-Siberian Sea.

2.3.3. Underway thermosalinographs (TSG)

Underway TSG data used in this study are recorded by 4 different vessels: the R/V Heincke, the R/V Polarstern, the R/V Mirai and the S/V Tara. Data of R/V Heincke and R/V Polarstern are downloaded on PANGAEA website (https://www.pangaea.de) and listed in the Appendix-B. R/V Mirai data of the year 2012 (JAMSTEC, 2013a), 2013 (JAMSTEC, 2013b) and 2014 (JAMSTEC, 2015) are downloaded on the DARWIN website of JAMSTEC (http://www.godac.jamstec.go.jp/darwin/e). S/V Tara measurements, that were quality checked at LOCEAN, are available on the Coriolis website. TSG measurements are taken at different depths, from 1 m on S/V Tara to 11 m for R/V Polarstern.

Underway TSGs salinities are the most variable (Fig. 1C). Their statistical distribution is characterized by three modes, a first mode is between 34 and 36 pss, a second mode between 31 and 32 pss and, finally, a third mode between 25 and 27 pss. Underway TSGs have a similar geographical sampling as CTD casts but with more measurements closer to coast and a better sampling of river plumes.

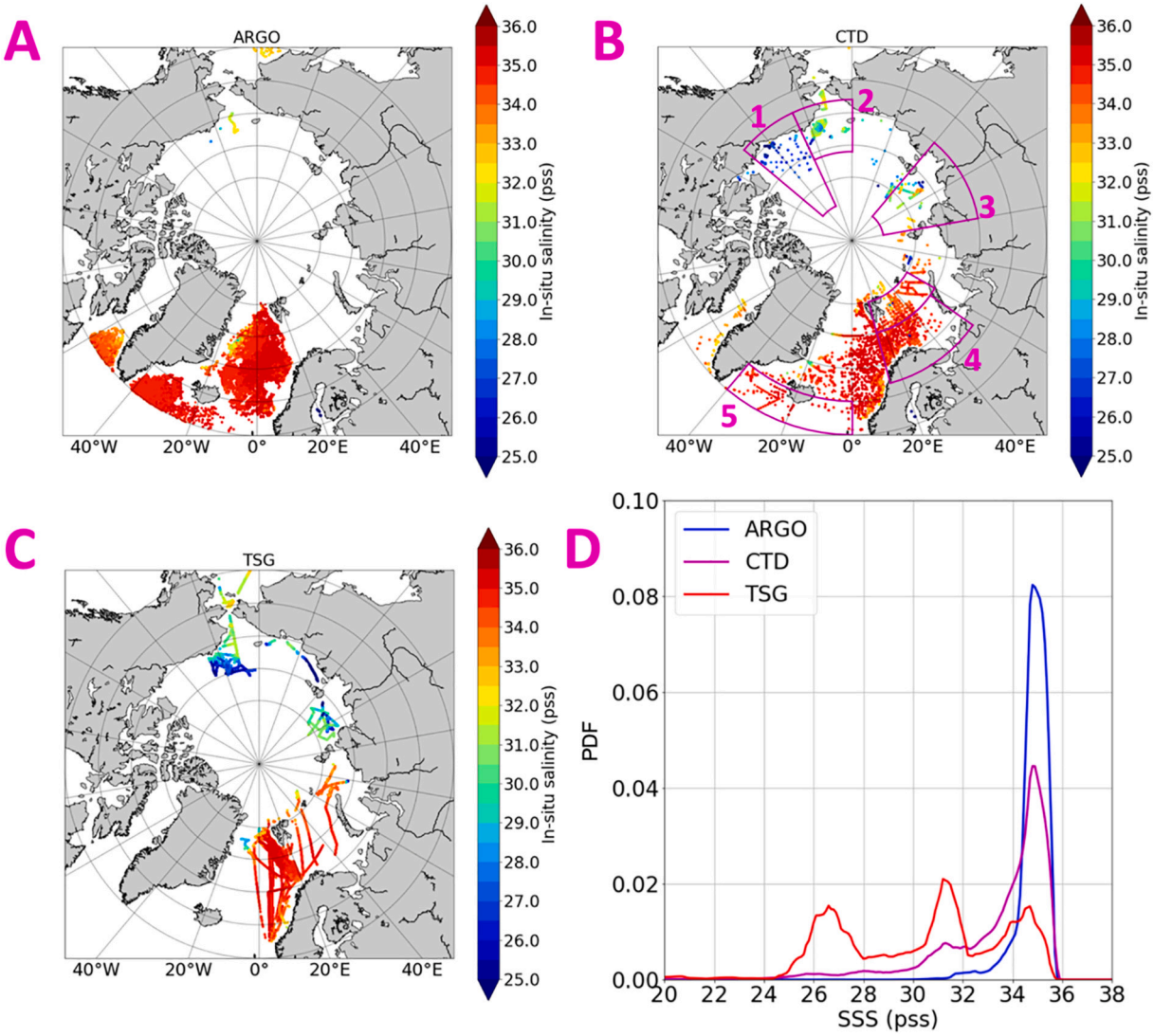

Fig. 1. In-Situ near-surface salinity measured at the location of (A) Argo floats (B) CTD casts in different study areas (1 - Beaufort Sea, 2 - Chukchi Sea, 3 - Laptev Sea, 4 - Barents Sea, 5 – Atlantic area) and (C) underway TSG. (D) Probability density function (PDF) of salinity observed with the different devices.

3. Influence of salinity vertical stratification on satellite/in-situ comparisons

3.1. Depth dependency: case of CTD profiles

We analyzed the effect of stratification on the differences between in-situ salinity (S_{insitu}) and SSS_{SMOS}. Fig. 2 presents the effect of stratification on mean comparisons between S_{insitu} and SSS_{SMOS} considering different depths. We consider here only CTD casts which provide the most complete depth and spatial coverage in the studied areas. Two cases are examined: cases with a difference lower than −0.1 pss between shallower (salinity average from 1 m to 5 m) and deeper levels (salinity average from 5 m to 10 m) named "stratified" cases ($\overline{S_{insitu\,[0m:5m]}} - \overline{S_{insitu\,[5m:10m]}} < -0.1\,pss$) and cases with a difference higher than −0.1 pss between shallower (salinity average from 1 m to 5 m) named "no-stratified" cases ($\overline{S_{insitu\,[0m:5m]}} - \overline{S_{insitu\,[5m:10m]}} > -0.1\,pss$). The −0.1 pss threshold is chosen arbitrary in a context of SSS validation. For "stratified cases", we observe a continuously increasing difference between S_{insitu} and SSS_{SMOS} with depth. In the "no-stratified" cases, as expected the difference is stable as a function of depth, but a slight difference remains between 1 m and 2 m depth (Fig. 2A). Stratified cases are mainly recorded over shelf seas and in river plumes areas (Fig. 2B). Cases without stratification are mainly recorded in the North Atlantic and Barents Sea. Considering 3228 CTD profiles: 81% are considered as not stratified whereas 19% are considered as stratified (Fig. 2C). Comparison of SSS_{SMOS} with S_{insitu} at all depths show a higher scatter for "no-stratified" cases than for stratified cases (Fig. 2D).

3.2. Study areas

In the present study, we focus our investigations on five study areas representing two inflow shelves with low stratification (Barents and Chukchi shelves), two more-stratified interior shelves (Laptev and Beaufort shelves) and an Atlantic area. The details are as follows:

- Beaufort Sea: between 155°W and 130°W and between 68°N and 84°N; the Beaufort Sea is characterized by the presence of the Beaufort gyre and a river plume from the Mackenzie river; the collocation dataset records the lower salinity values in the Beaufort Sea;
- Chukchi Sea: between 68°N and 76°N and between 155°W and 180°W; the Chukchi Sea is a shallow sea dominated by a freshwater inflow from the Pacific Ocean;

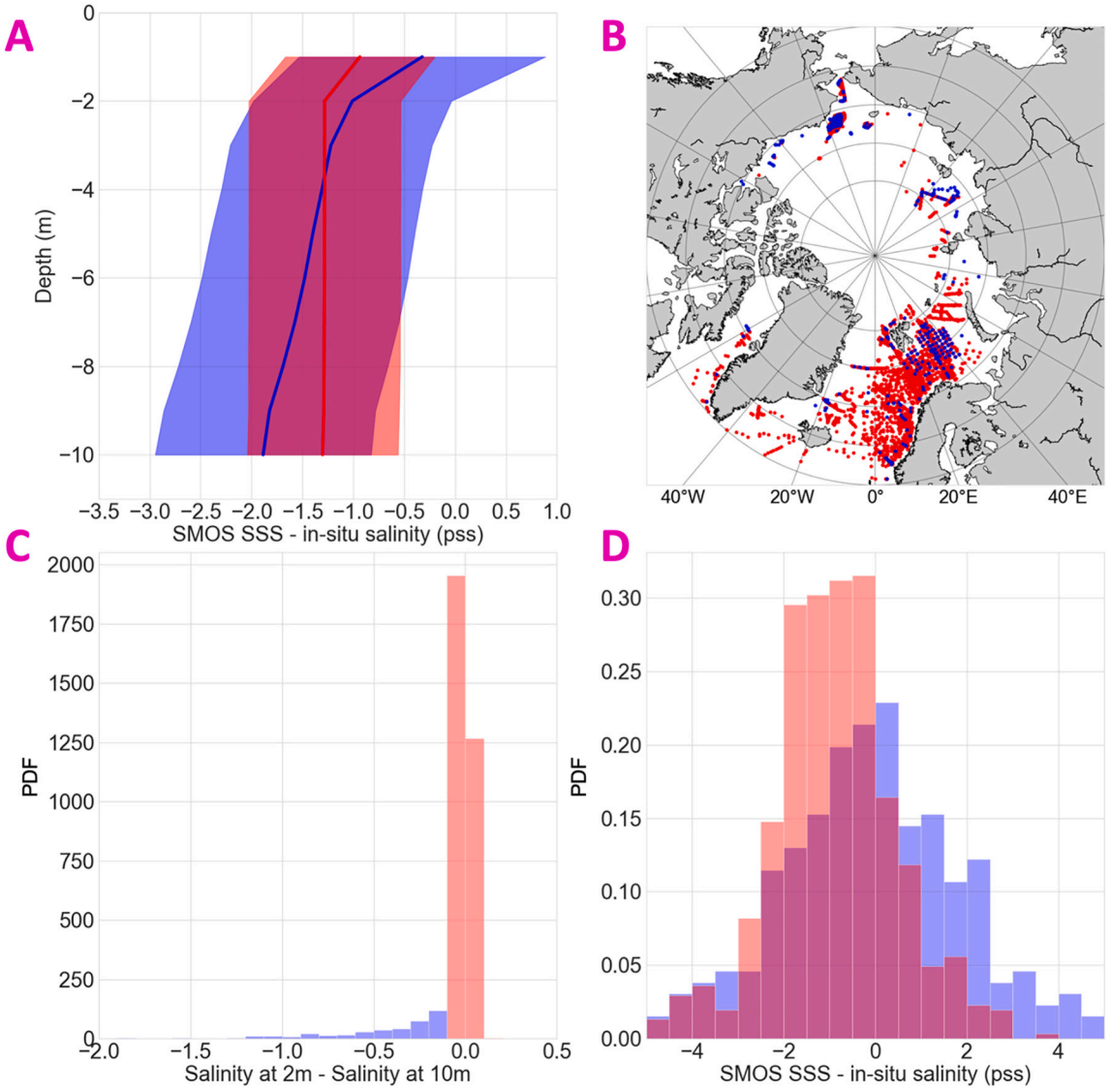

Fig. 2. (A) Averaged differences between S_{insitu} and SSS_{SMOS} as a function of depth in stratified and not-stratified cases (shaded area represents 2 × standard deviation); (B) Geographical distribution of stratified and not stratified cases; (C) Statistical distribution of differences between shallower (salinity average from 1 m to 5 m) and deeper levels (salinity average from 5 m to 10 m) for different CTD profiles; (D) Statistical distribution of differences between SSS_{SMOS} and in-situ salinity for stratified and not-stratified cases. "Stratified cases" ($\overline{S_{insitu[0m:5m]}} - \overline{S_{insitu[5m:10m]}} < -0.1\ pss$) are in blue and "not-stratified" cases ($\overline{S_{insitu[0m:5m]}} - \overline{S_{insitu[5m:10m]}} > -0.1\ pss$) are in red. (For interpretation of the references to colour in this figure legend, the reader is referred to the web version of this article.)

- Laptev Sea: between 100°E and 140°E; the Laptev Sea is influenced by freshwater from the Lena river plume, an inflow of freshwater from the Kara Sea, and salty water from the Atlantic Ocean above the continental slope;
- Barents Sea: between 75° and 80° N and between 15°E and 60°E; and between 60°E and 67°N and between15°E and 55°E; the Barents Sea is dominated by inflow from the Atlantic characterized by salty waters with respect to other study areas. The SSS variability of this area is less pronounced than in the previous areas.
- Atlantic area: between 60°N and 65°N and between 40°W and 0°W; this area represents the highest SSS of the study and the lowest variability of the SSS.

The depth of the in-situ measurement plays a different role in different areas. Figs. 3 and 4 compare CTD measurements with SSS_{SMOS} for each study area. In the salty regions (Barents Sea and Atlantic area, Fig. 3), the depth of in-situ measurements does not seem to influence strongly the relationship between S_{insitu} and SSS_{SMOS}. These areas demonstrate very stable mean (MoD) and STD (STDD) difference between S_{insitu} and SSS_{SMOS}.

In fresher regions (Fig. 5), in the Beaufort and Laptev Sea (Figs. 4A, B and 4E, F), where the runoff of the Mackenzie and the Lena river are observed, important differences between SSS_{SMOS} and in-situ measurements are observed when the depth of the in-situ measurement increases. In the Laptev Sea, it is even stronger when the surface salinity is lower, indicating a stronger stratification. In the Chukchi Sea (Fig. 4C, D), the stratification effect is less pronounced than in the Beaufort and the Laptev Seas. Figs. 3 and 4 clearly show that, as expected, stratification increases when the observed surface salinity decreases. In the Beaufort Sea, the average difference between 1 m and 10 m depth is −1.84 pss (Fig. 4B). In the Laptev Sea, average difference between 2 m and 10 m depth is −1.47 pss (Fig. 4F). The STDD between SSS_{SMOS} and S_{insitu} is also strongly affected by the stratification: in the Beaufort Sea STDD increase from 1.47 pss (1 m depth) to 2.29 pss (10 m depth) and from 1.83 pss (2 m depth) to 2.12 pss (10 m depth) in the Laptev Sea.

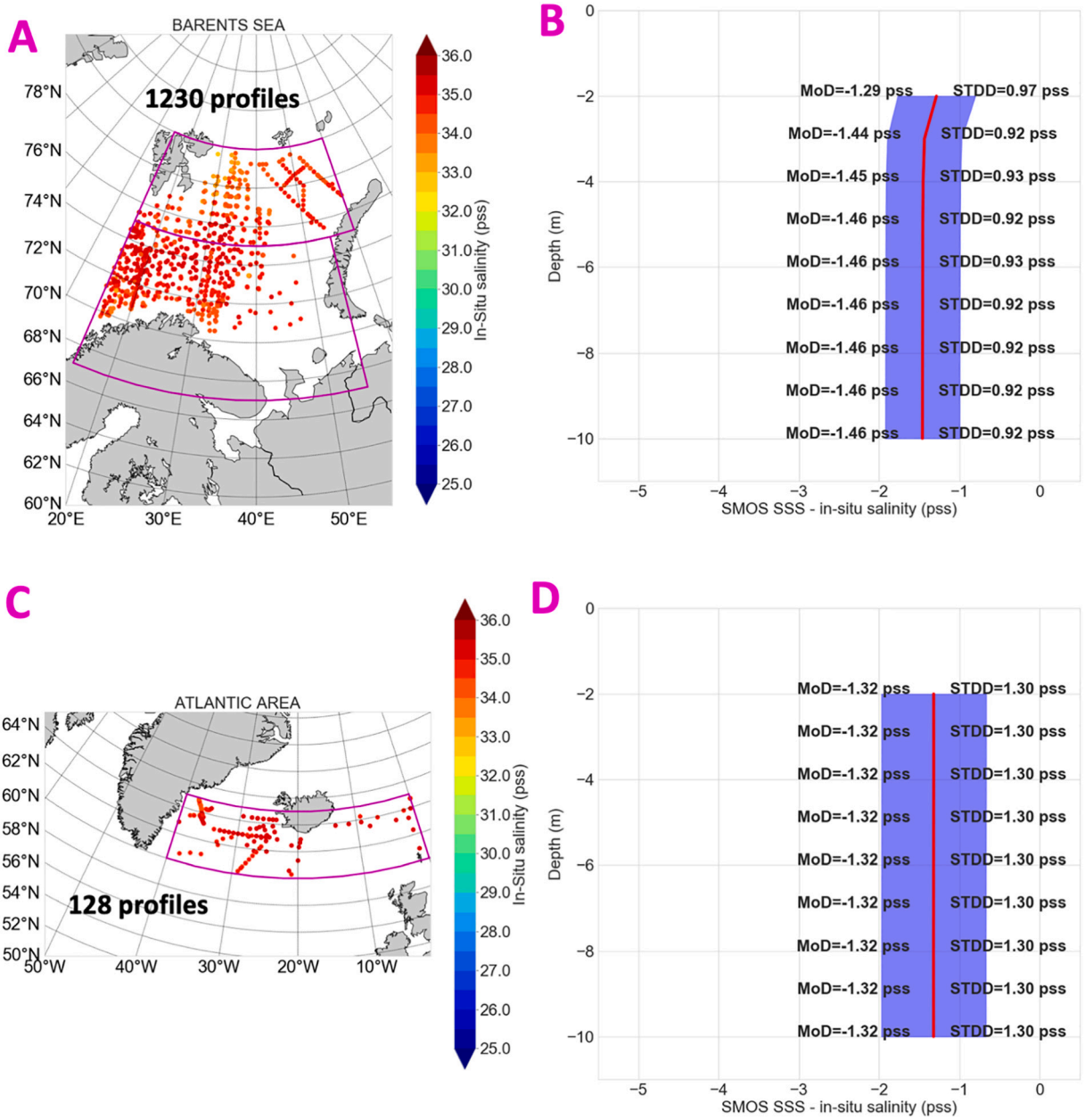

Fig. 3. Effect of stratification on relationship between SSS_{SMOS} and in-situ salinity measurements in salty regions: (A, C) coordinates of colocalizations between SMOS and CTD profiles in different study areas (Barents Sea, Atlantic area); (B, D) MoD between SSS_{SMOS} and in-situ salinity for different depths (from CTD casts only, with shaded area representing 2 standard deviation).

3.3. Selection of in-situ measurements for absolute SSS calibration and validation

The selection of S_{insitu} for comparison and validation with satellite SSS is a compromise between the need for a set of in-situ measurements representative of the whole Artic Ocean and the need for in-situ measurements representative of SMOS estimates (1 cm depth).

We select S_{insitu} according to depth in order to avoid as much as possible the effect of vertical stratification. However, in situ measurements between 1 m and 5 m depth cover much broader regions and in particular fresh areas not sampled by in situ measurements between 1 m and 3 m depth (Appendix-C). Hence, for the validation purpose (section 5.2), the maximum depth of S_{insitu} is set at 5 m.

On the other hand, the absolute calibration (constant bias removal) of SMOS SSS is performed in a salty area less prone to stratification effects, the Barents Sea, where we only consider the uppermost S_{insitu}.

4. Novel corrections and filtering: methodology

4.1. Sea ice and outliers filtering: Acard

A main contamination of satellite SSS at high latitude comes from the presence of sea ice (Tang et al., 2018) which emissivity is much higher than the one of the surface ocean due to a much lower dielectric constant. Our filtering procedure will take advantage of L3 Acard.

Acard may be retrieved directly from SMOS TB and a prior SST, considering only emissivity and Fresnel equations, independently from the dielectric constant model (Table 1). It is named $Acard_{SMOS}$ below. It is also possible to compute Acard ($Acard_{KS}$) from a theoretical dielectric constant model using eq. [A2] (Appendix-A). We use the KS dielectric constant model also used to retrieve SSS in the L2 OS processor. The difference between $Acard_{SMOS}$ and $Acard_{KS\ (SMOS\ SSS,\ ECMWF\ SST)}$ ($D_{Acard} = Acard_{SMOS} - Acard_{KS\ (SMOS\ SSS,\ ECMWF\ SST)}$) may result from

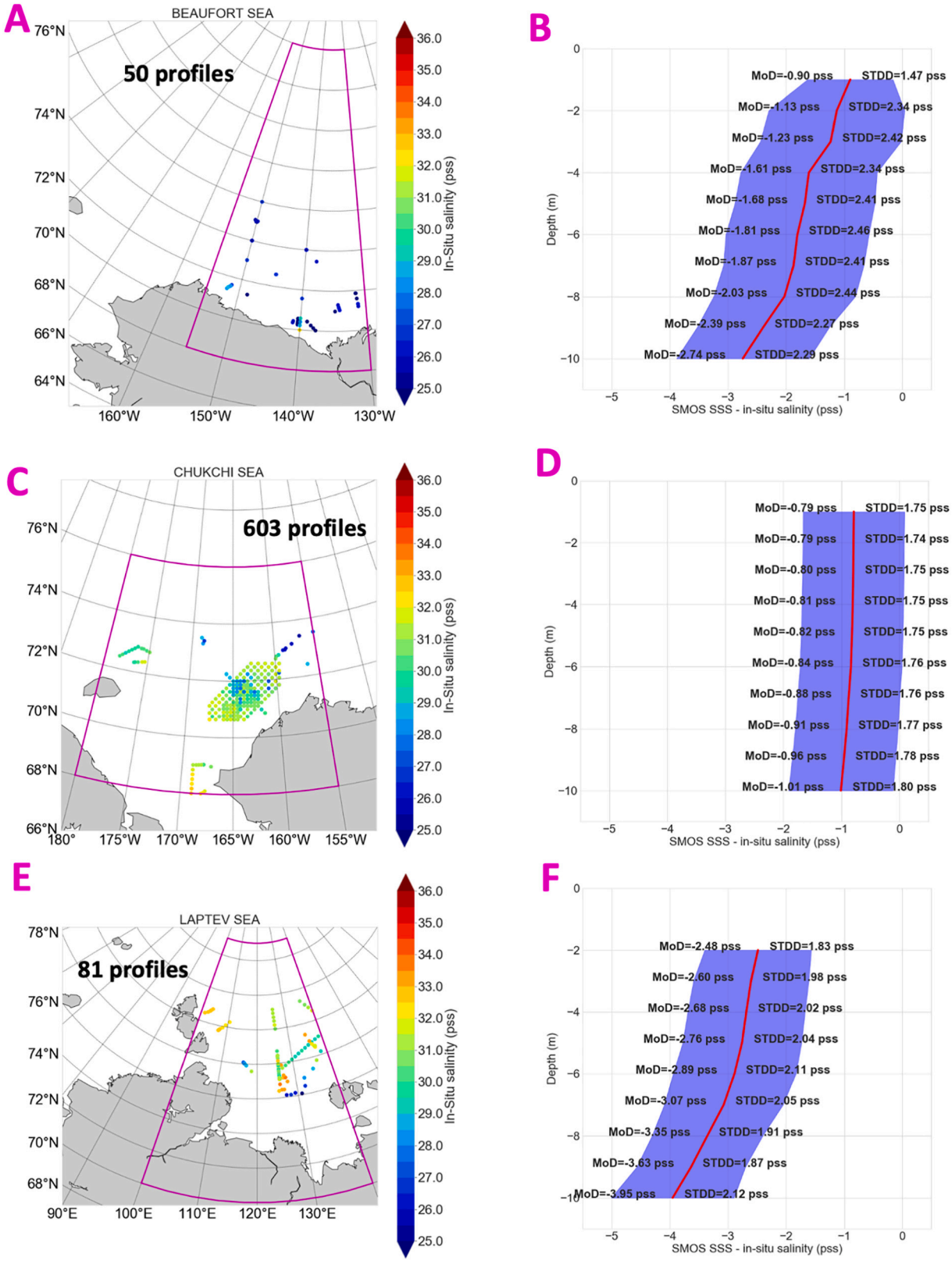

Fig. 4. Effect of stratification on the relationship between SSS_{SMOS} and in-situ salinity measurements in fresh regions: (A, C, E) coordinates of colocalizations between SMOS and CTD profiles in the different study areas (Beaufort Sea, Chukchi Sea, Laptev Sea); (B, D, F) MoD between SSS_{SMOS} and in-situ salinity for different depths (from CTD casts only, with shaded area representing 2 standard deviation).

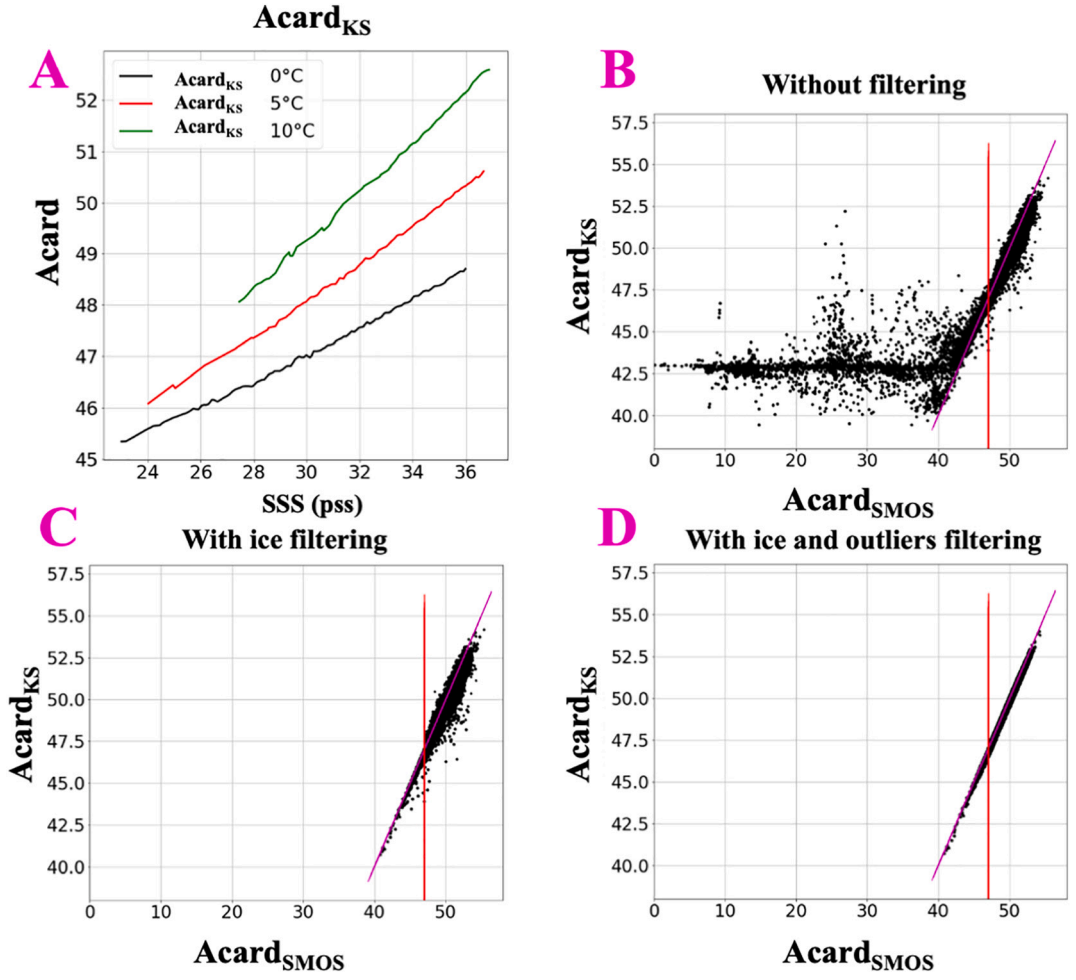

Fig. 5. (A) Relationship between Acard and SSS at various SST considering KS model; (B) Scatterplot of $Acard_{KS}$ versus $Acard_{SMOS}$ without filtering; (C) same as (B) with ice filtering (first step); (D) same as (B) with ice filtering and outliers filtering (second step); (red) $Acard_{SMOS}$ = 47 threshold; (magenta) line corresponding to $Acard_{KS}$ = $Acard_{SMOS}$. (For interpretation of the references to colour in this figure legend, the reader is referred to the web version of this article.)

either:

- an imperfect representation of the dielectric properties of the observed surface by the KS model, or,
- uncertainties on the SSS and SST priors used to compute $Acard_{KS}$, or,
- residual errors in the correction of atmospheric, solar and sky glint, or sea surface roughness used to estimate the flat sea surface radiobrightness contrast, or,
- And/or from corrupted SMOS TB (RFI, image reconstruction errors, etc.) used to retrieved $Acard_{SMOS}$.

In the following, we address uncertainties coming from the first two items. We compute $Acard_{KS}$ using retrieved SMOS SSS and ECMWF SST ($Acard_{KS\ (SMOS\ SSS,\ ECMWF\ SST)}$). Fig. 5A illustrates the relationship between SSS and Acard for different SST. Academic simulations (not shown) suggest that $Acard_{SMOS}$ is much lower than $Acard_{KS\ (SMOS\ SSS,\ ECMWF\ SST)}$ when sea ice is present within a SMOS pixel.

Based on these considerations, we developed a two-step filtering methodology. As illustrated in Fig. 5B which represents $Acard_{SMOS}$ as a function of $Acard_{KS\ (SMOS\ SSS,\ ECMWF\ SST)}$ without applying any filtering: two main regimes are observed. The first regime (points on the diagonal, above 40, Fig. 5B), corresponds to the expected behavior between $Acard_{SMOS}$ and $Acard_{KS\ (SMOS\ SSS,\ ECMWF\ SST)}$ in the absence of sea ice. The second regime (plateau in $Acard_{KS}$, below 40, Fig. 5B) with large differences between $Acard_{SMOS}$ and $Acard_{KS\ (SMOS\ SSS,\ ECMWF\ SST)}$ is due to pixel partially covered by sea ice and/or an inappropriate use of KS in order to compute Acard in these cases (KS model is designed for sea ice free ocean conditions). We note that the probability to observe the second regime case strongly increases with an Acard value lower than 47. In a first step, when Acard is less than 47, we apply a very restrictive filter by removing all pixels with a D_{Acard} value lower than −0.1 (Fig. 5C). In a second step, we filter out D_{Acard} values lower than −0.21 and larger than 0.52, that correspond respectively to the 0.05 and 0.95 percentiles of D_{Acard} distribution after ice filtering (Fig. 5D).

4.2. Absolute calibration of SSS

Considering differences with respect to upper S_{insitu} in the Barents Sea (Fig. 3B), we add 1.29 pss to SMOS SSS for removing the SMOS SSS global bias.

4.3. Correction related to uncertainty on the dielectric constant model

Flaws in the dielectric constant model may lead to errors on both the retrieved SSS_{SMOS} and SST_{SMOS} (as defined in Table 1) but not on $Acard_{SMOS}$ since the Acard retrieval is independent of any dielectric constant model. As a first approximation, we assume that errors in the dielectric model only induce biases in the retrieved SSS_{SMOS} and not on

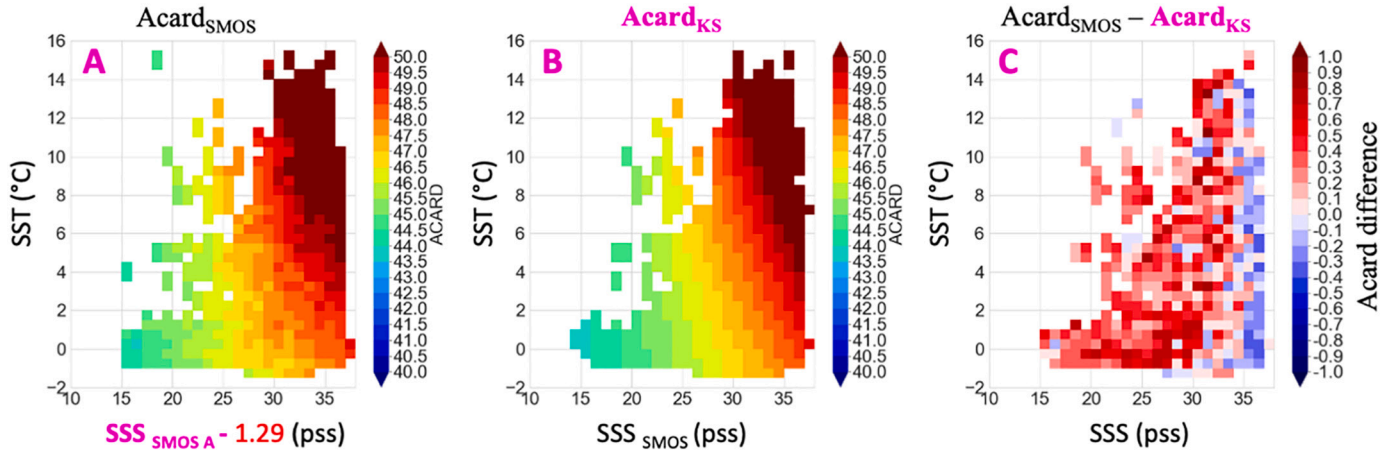

Fig. 6. (A) $Acard_{SMOS}$ as a function of SST_{ECMWF} and $SSS_{SMOS\ A}$ – 1.29 $Acard_{KS(SMOS\ SSS,ECMWF\ SST)}$; (B) $Acard_{KS(SMOS\ SSS,ECMWF\ SST)}$ as a function of SST_{ECMWF} and SSS_{SMOS}; (C) Difference between $Acard_{SMOS}$ and $Acard_{KS}$. SMOS retrieved variables are in black, computed variables are in magenta. (For interpretation of the references to colour in this figure legend, the reader is referred to the web version of this article.)

retrieved SST. We compare $Acard_{SMOS}$ with $Acard_{KS}$ computed with parameters available in the SMOS User Data Product, i.e. SSS_{SMOS} and SST_{ECMWF}. A first correction on SSS_{SMOS} can then be determined using the following relationship that also consider absolute calibration (section 4.2.):

$$SSS_{SMOS\ A} = SSS_{SMOS} + \frac{(Acard_{KS} - Acard_{SMOS})}{\lambda(SST_{ECMWF},\ SSS_{SMOS})} + 1.29 \quad (2)$$

where

$$\lambda(SST, SSS) = \frac{\partial Acard_{KS}(SST, SSS)}{\partial SSS}.$$

Fig. 8 shows differences between $Acard_{SMOS}$ and $Acard_{KS}$. $Acard_{SMOS}$ is plotted as a function of SST and $SSS_{SMOS\ A}$ - 1.29 in order to be comparable to $Acard_{KS}$ computed with SSS_{SMOS} (Fig. 6A). Differences between $Acard_{SMOS}$ and $Acard_{KS}$ are larger for low SSS and low SST (Fig. 6C). This correction integrates different biases that can not be disentangled in this study: 1) SSS bias coming from the KS model; 2) SSS bias due to a potential difference between SST retrieved with SMOS and SST_{ECMWF}.

4.4. Correction linked to uncertainty on prior SST

We observe that in some regions such as the Lena river plume in the Laptev Sea, SST_{ECMWF} is nevertheless underestimated with respect to upper in-situ temperature, T_{insitu}. As shown in Appendix-D (Fig. D1), stronger SST gradient are observed in REMSS SST product compared with OSTIA SST used in ECMWF. Based on the KS model, it is possible to compute a second correction of the retrieved SSS considering sensitivity to SST and selecting another SST product as reference (here chosen to be REMSS SST):

$$SSS_{SMOS\ A+T} = SSS_{SMOS\ A} + \frac{\gamma(SST_{ECMWF}SSS_{SMOS})}{\beta(SST_{ECMWF}SSS_{SMOS})}(SST_{ECMWF} - SST_{REMSS}) \quad (3)$$

$$\text{where } \beta(SST, SSS) = \frac{\partial TB(SST, SSS)}{\partial SSS} \text{and } \gamma(SST, SSS) = \frac{\partial TB(SST, SSS)}{\partial SST}.$$

5. Results and validation

5.1. Validation of sea ice filtering

To assess the efficiency of the Acard filtering for sea ice we used SIC data from TOPAZ and we analyze a case study in the Laptev Sea. As illustrated on Fig. 7, without the Acard filtering, low SSS values are observed in the northernmost areas in the vicinity of sea ice edges because of a too permissive filtering of ice in the ESA L2 processor. At these locations, negative D_{Acard} and positive SIC from TOPAZ are observed.

Over the whole Arctic Ocean and period investigated (Fig. 8), Acard ice filtering removes all pixels with SIC larger than 2.5% and most pixels with SIC in the range of 0%–2.5%. MoD and STDD with respect to in-situ SSS significantly decrease after filtering and do not show a dependency to TOPAZ SIC anymore suggesting that the remaining SMOS pixels are not significantly polluted by sea ice. These results demonstrate the efficiency of Acard ice filtering over using an external SIC product. Hereafter, we refer to SSS_{SMOS} as the SMOS SSS obtained after the above described processing. SSS_{SMOS} considered in the following are therefore sea ice filtered.

5.2. Validation of the SSS product

The main motivation for the temperature-dependent correction is found in the distribution of SST. As shown in Fig. 9, SST_{REMSS} are closer to in-situ SST than SST_{ECMWF}. Depending on the Arctic Ocean regions considered, two modes are generally present in both the distribution of SST_{REMSS} and in-situ SST (Fig. 10 and 11) but the mode corresponding to higher temperatures is almost absent in the SST_{ECMWF} distribution.

In order to make a realistic comparison of the statistical distributions of SMOS and in situ SSS, in each area we add noise to S_{insitu} to mimic SMOS noise, considering a Gaussian noise being derived from the theoretical uncertainty of the collocated SMOS L3 SSS.

The positive effect of the correction is clear in Chukchi and Laptev Seas. For these two regions, SST_{ECMWF} distribution clearly underestimates the warmest SST mode (Figs. 10H, I) in comparison with REMSS, or, T_{insitu}. This results into a distribution of SMOS SSS without the SST_{REMSS} correction showing an important number of underestimated SMOS SSS (Fig. 10B, C). This correction results in a distribution of SMOS SSS closer to the S_{insitu} distribution (Figs. 10E, F), thus the STDD and MoD decrease and the correlation coefficient (r) increases (Table 2) for the Chukchi Sea and the Laptev Sea.

To a lower extent, the same kind of difference is observed in the Beaufort Sea (Figs. 10A, D, G). In the Barents Sea, the SST_{ECMWF} distribution is closer to that of T_{insitu} and SST_{REMSS} than for the other study areas and our correction only brings a very small improvement (Figs. 11A, D, G and STDD in Table 1). Finally, the Atlantic area presents a degradation of SSS after Acard difference and SST corrections (Figs. 11B, E, H and STDD in Table 2). This is mainly due to the Acard correction (Appendix-E). Indeed, this correction assumes that error in

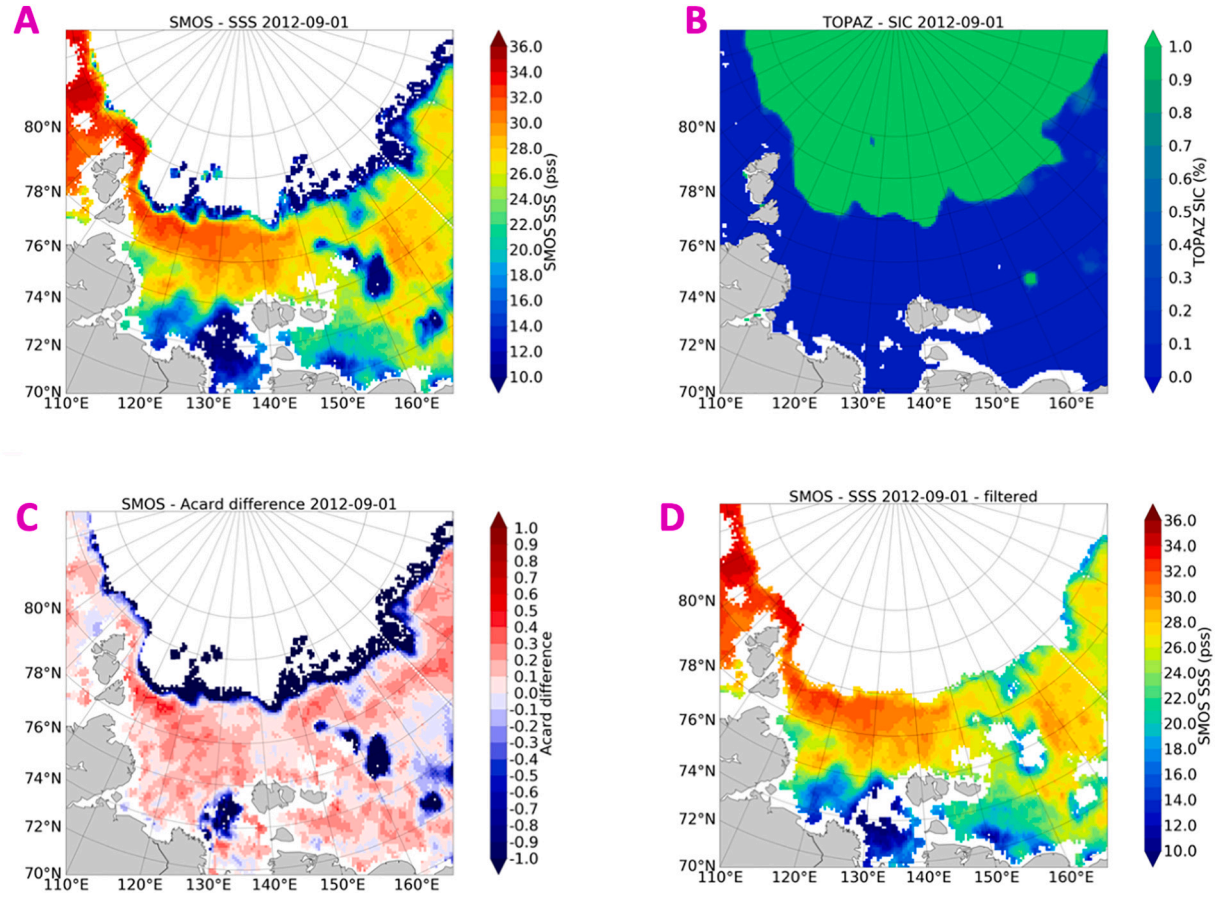

Fig. 7. L3 post-processing flagging for the study case of 2012-09-01: (A) SMOS SSS pre-processed L3 estimates; (B) TOPAZ reanalysis SIC; (C) differences between $Acard_{SMOS}$ and $Acard_{KS\ (SMOS\ SSS,\ ECMWF\ SST)}$; (D) SMOS SSS estimates after filtering.

the SSS estimation comes from errors in dielectric constant model and/or from erroneous prior SST. In the Atlantic area, RFI likely disturb TB such that their angular variation cannot be described with a Fresnel model, and therefore our correction is not appropriate.

Considering the whole Arctic Ocean (Figs. 11C, F, I), the distribution of the corrected SMOS SSS fits better S_{insitu}. After correction, the STDD and MoD improve from 1.46 pss to 1.28 pss and from −1.54 pss to −0.27 pss, respectively; r increases from 0.92 to 0.94 (Table 2).

Over the whole Arctic Ocean, the difference between SST_{REMSS} and T_{insitu} is less than the difference observed between SST_{ECMWF} and T_{insitu}. The difference SST_{ECMWF} - T_{insitu} exceeds −1 °C for T_{insitu} between 3 °C and 4 °C, temperatures that are often present in the Arctic Ocean (Figs. 9 and 11I). In this SST range, the correction is efficient to reduce the satellite SSS differences with respect to T_{insitu}. The overestimation of SST observed with both ECMWF and REMSS products for SST lower than 0 °C (Fig. 9) should lead to an overestimation of SSS (Fig. 12).

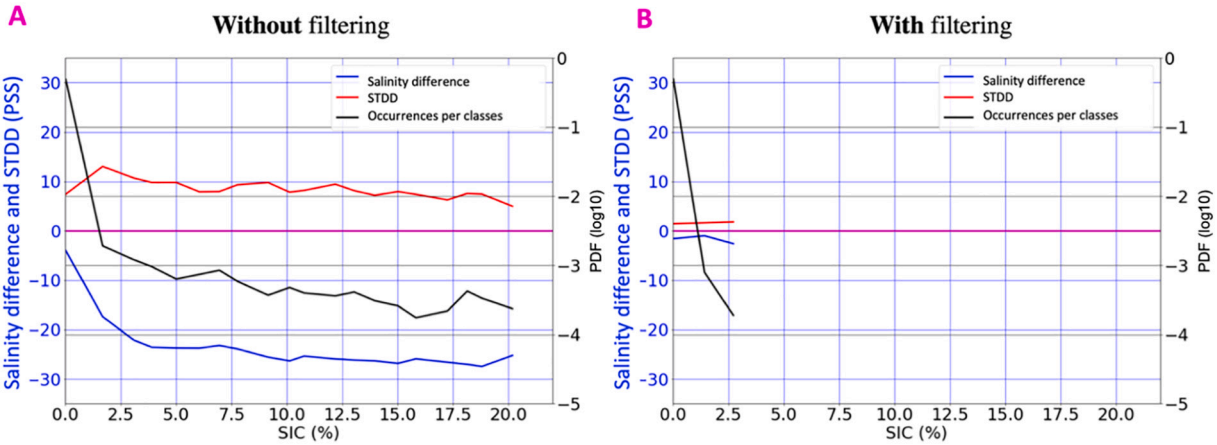

Fig. 8. Mean difference and STDD between SMOS SSS and in-situ salinity and PDF of collocations per bin (bin size: 1%) of TOPAZ SIC; (A) without filtering; (B) with filtering.

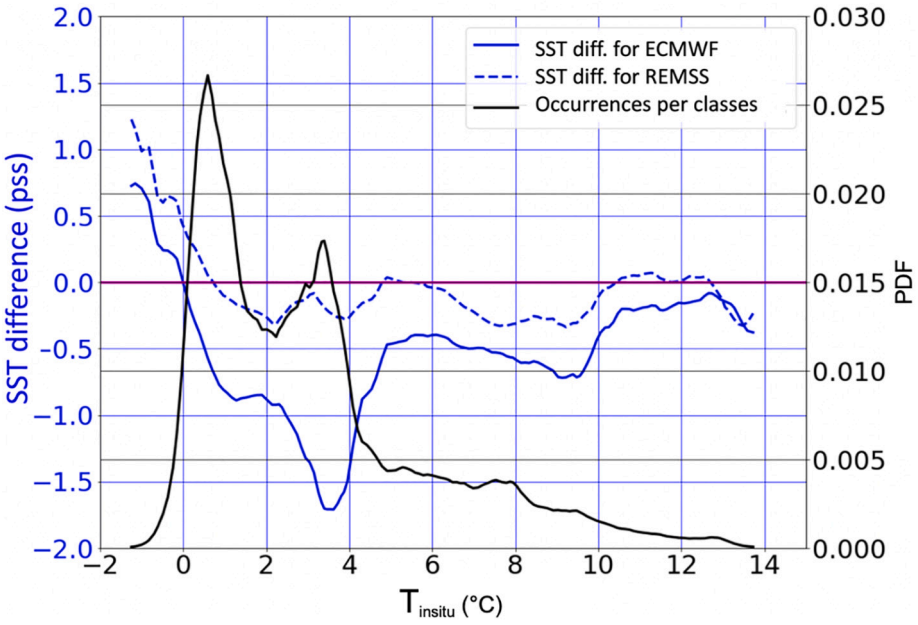

Fig. 9. Difference of SST_{ECMWF} – T_{insitu} (blue line) and SST_{REMSS} - T_{insitu} (blue dashed line) as a function of T_{insitu}. Distribution of T_{insitu} (black line); (bin size: 1 °C – sliding window). (For interpretation of the references to colour in this figure legend, the reader is referred to the web version of this article.)

However, an underestimation of SSS is observed for the coldest surface temperatures without any link with SST difference, likely due to some remaining very low sea ice concentration or very near surface freshening close to sea ice unidentified with in-situ measurements.

6. Comparisons between SMOS SSS and TOPAZ SSS

6.1. Weekly variability

To assess the capability of the corrected SMOS SSS products to reproduce the short scale SSS variability in the Arctic relative to an ocean circulation model, we compare hereafter $SSS_{SMOS\ A+T}$ and SSS_{TOPAZ} (Table 3) to a reference salinity provided by underway TSG tracks acquired in three different seas: Greenland Sea (case study 1), Laptev Sea (case study 2) and Chukchi Sea (case study 3). For the case study in the Greenland Sea, the vessel is arriving from an area covered by sea ice. It first crosses an area of low salinity before an area with SSS ~ 35 pss. Both $SSS_{SMOS\ A+T}$ and SSS_{TOPAZ} do not reach the lower values recorded by the TSG (Fig. 13A, B). Only one $SSS_{SMOS\ A+T}$ pixel reaches a value lower than 26 pss, but an effect of ice may not be excluded even if the SIC from TOPAZ indicates no ice. $SSS_{SMOS\ A+T}$ exhibits better STDD and MoD than SSS_{TOPAZ} with respect to the TSG. For the study case in the Laptev Sea (Fig. 13C and 13D), $SSS_{SMOS\ A+T}$ show a positive bias (larger than SSS_{TOPAZ}) for higher SSS values recorded by the TSG contrary to SSS_{TOPAZ} which fits well with these salinities. However, the large freshening (more than 10 pss) observed by the vessel crossing the Lena river plume is very well represented by $SSS_{SMOS\ A+T}$ contrary to SSS_{TOPAZ}, which misses the location of the river plume and its intensity. Nevertheless, $SSS_{SMOS\ A+T}$ demonstrates in this case a higher STDD than SSS_{TOPAZ}. In the Chukchi Sea (Fig. 13E and 13F), the underway TSG presents a large variability also observed by $SSS_{SMOS\ A+T}$ but with some bias. This variability is not recorded by SSS_{TOPAZ}. The STDD and bias with respect in situ data, are lower with $SSS_{SMOS\ A+T}$ than with SSS_{TOPAZ} by ~0.2 and 0.3, respectively.

In Fig. 14, $SSS_{SMOS\ A+T}$ and SSS_{TOPAZ} distributions are compared with S_{insitu} distributions over the whole Arctic Ocean. The distribution of $SSS_{SMOS\ A+T}$ compares very well with the distribution of S_{insitu} (Fig. 14A). One mode of the S_{insitu} distribution (lower SSS) is totally absent in the SSS_{TOPAZ} distribution. STDD (Table 2) is 1.28 pss for $SSS_{SMOS\ A+T}$ and 1.86 pss for SSS_{TOPAZ}. r reaches 0.94 with $SSS_{SMOS\ A+T}$ while it is 0.89 with SSS_{TOPAZ}. The distribution of errors for $SSS_{SMOS\ A+T}$ presents only one mode contrary to SSS_{TOPAZ} that present two modes due to the absence of the lower SSS (Fig. 14B).

The scatterplot of $SSS_{SMOS\ A+T}$ versus S_{insitu} further indicates an overall agreement between SSS estimates from space and in-situ measurements. In addition, the SMOS SSS uncertainty estimated in the L3 product (see section 2.1.2) seems to be a good indicator of the quality of the considered $SSS_{SMOS\ A+T}$ estimate.

6.2. Interannual variability

We then compare the $SSS_{SMOS\ A+T}$ interannual variability to SSS_{TOPAZ} interannual variability. For each year between 2011 and 2017 we average SSS between August and October in order to consider the season with the lowest sea ice coverage in the Arctic Ocean. The average is weighted by the uncertainty value of each L3 SSS estimate. Fig. 15 is a comparison for the 2012, 2013 and 2014 years and Fig. 16 is a comparison for the 2015, 2016 and 2017 years. Contrary to TOPAZ that provides an SSS value for each pixel of the Arctic Ocean, $SSS_{SMOS\ A+T}$ coverage depends on the sea ice extent. For the comparison we take into account SSS_{TOPAZ} only when a $SSS_{SMOS\ A+T}$ value exists.

A good overall consistency in the Arctic Ocean is observed between $SSS_{SMOS\ A+T}$ and SSS_{TOPAZ} interannual variations. However, $SSS_{SMOS\ A+T}$ exhibits a higher interannual and spatial variability than SSS_{TOPAZ}. Furthermore, some areas behave differently with $SSS_{SMOS\ A+T}$ in comparison with SSS_{TOPAZ}. For the whole period and as observed previously regarding S_{insitu} (Table 2), the freshening of the Beaufort gyre is strongly underestimated with SSS_{TOPAZ} compared to $SSS_{SMOS\ A+T}$. The

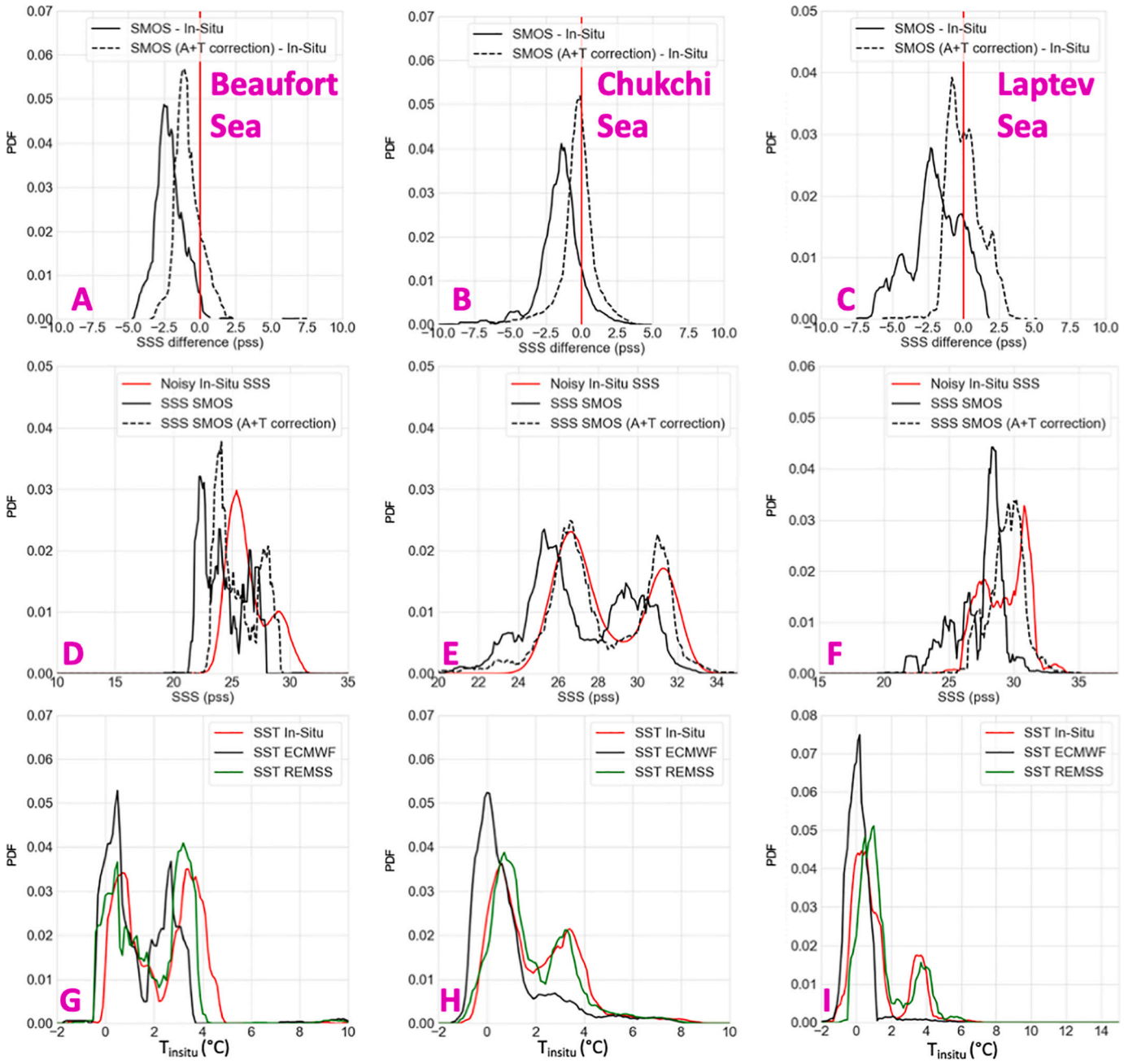

Fig. 10. (A, B, C) Distribution of SMOS SSS minus S_{insitu} without correction (black line) and with correction (dashed line) for the different study areas and for the whole Arctic Ocean (1 pss SSS difference bin – sliding window); (D, E, F) distribution of SSS_{SMOS} (black line), $SSS_{SMOS\ A+T}$ (dashed line) and noisy (using SSS_{SMOS} theoretical uncertainty) S_{insitu} (red line) for the different study areas and for the whole Arctic Ocean (1 pss salinity bin – sliding window); (G, H, I) In-Situ (red), ECMWF (black) and REMSS (green) SST distributions (1 °C SST bin – sliding window). Low salinity study areas: (A, D, G): Beaufort Sea; (B, E, H): Chukchi Sea; (C, F, I) Laptev Sea.

variability and spatial extent of Arctic Ocean river plumes also differ strongly between SSS_{TOPAZ} and $SSS_{SMOS\ A+T}$. In the Kara Sea, the locations and strength of the Ob and the Yenissei river plumes are highly variable from one year to the other (freshening minimum in 2012 and 2016, maximum in 2015). This variability is captured by SSS_{TOPAZ} and $SSS_{SMOS\ A+T}$, but with larger amplitudes in $SSS_{SMOS\ A+T}$, in particular in 2015. River plume propagation to the north or/and to the east in the East-Siberian Sea are not captured in the same way by SSS_{TOPAZ} and $SSS_{SMOS\ A+T}$. For example, in 2015, the strong northward advection of Lena river plume shown by $SSS_{SMOS\ A+T}$ is not observed with SSS_{TOPAZ}. Similar observations are made in the Bering strait with the entry of Pacific water or low SSS water in the Greenland Sea and in the Baffin Bay.

Contrary to SSS_{TOPAZ}, freshening patterns are observed at the northern boundary of the field covered by $SSS_{SMOS\ A+T}$ (limitation due to the presence of permanent ice). The cause of this freshening is not

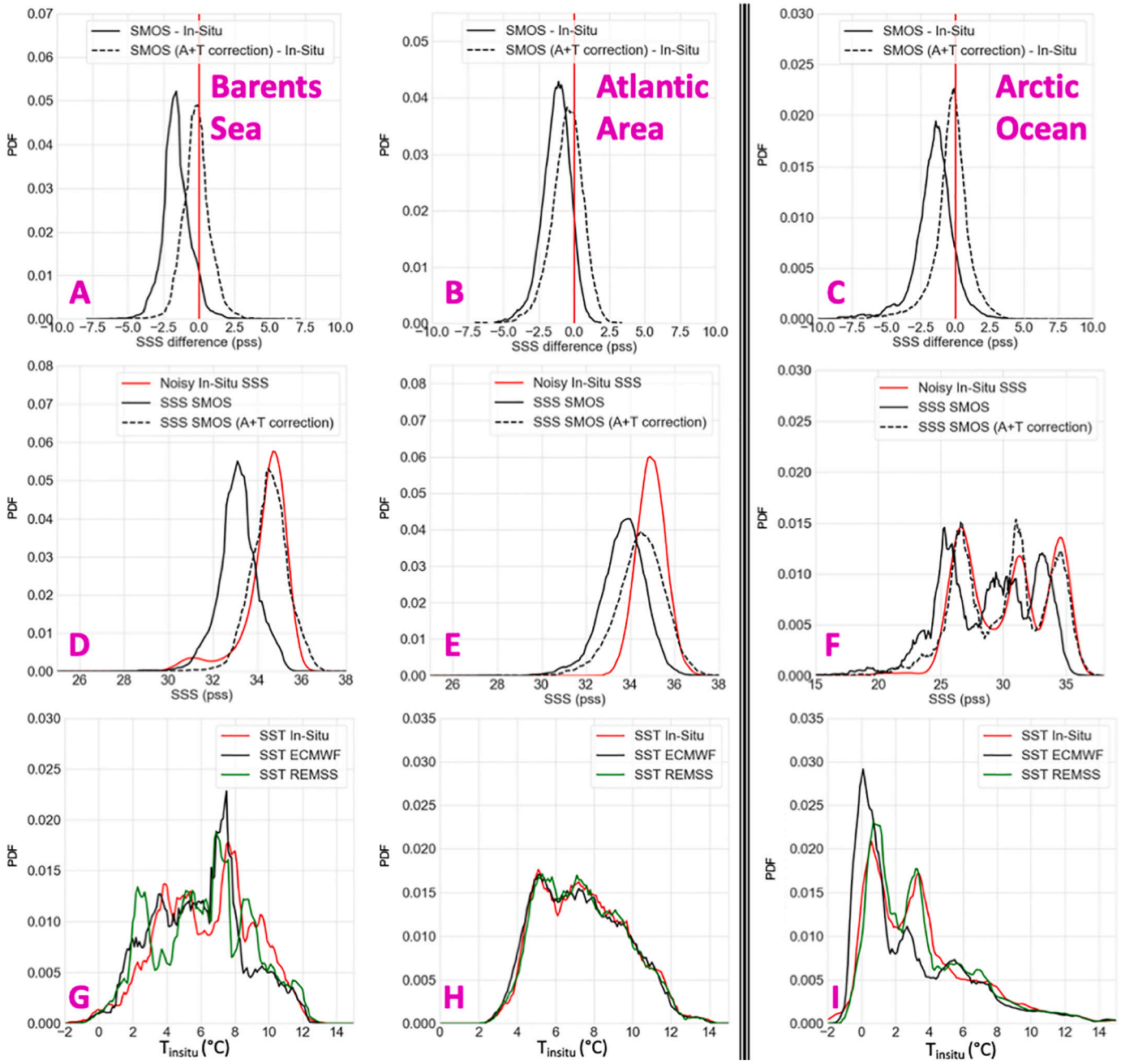

Fig. 11. (A, B, C) Distribution of SMOS SSS minus S_{insitu} without correction (black line) and with correction (dashed line) for the different study areas and for the whole Arctic Ocean (1 pss SSS difference bin – sliding window); (D, E, F) distribution of SSS_{SMOS} (black line), $SSS_{SMOS\ A+T}$ (dashed line) and noisy (using SSS_{SMOS} theoretical uncertainty) S_{insitu} (1 pss salinity bin – sliding window); (G, H, I) In-Situ (red), ECMWF (black) and REMSS (green) SST distributions (1 °C SST bin – sliding window). High salinity study areas: (A, D, G) Barents Sea, (B, E, H) Atlantic Area, and (C, F, I) the whole Arctic Ocean.

totally explained and may come from a real freshening due to ice melting or an imprint of sea ice due to an imperfect filtering of sea ice.

7. Conclusion and discussion

We present a methodology that significantly improves SSS estimates in the Arctic Ocean. It is applied to SMOS L3 SSS derived from ESA level 2 operational processing (L2 OS v662).

In a first step, the difference between a pseudo dielectric constant, Acard, retrieved from SMOS measurements and a theoretical Acard estimated with KS model is used to efficiently filter out biased SSS in pixels partially covered by sea ice.

A global correction (1.29 pss) over the whole Arctic Ocean is applied, to take into account the uncertainty associated with the absolute calibration of the measurements.

The Acard difference is then used as a metric of the biases in the KS model for the dielectric constant of sea water. An additional SST correction derived using an external SST satellite product, SST_{REMSS}, is performed. The latter is motivated by observed difference of statistical distribution between SST_{ECMWF} (which is used in the retrieval of SSS)

Table 2
Comparisons between SMOS SSS, without and with correction, TOPAZ SSS and S_{insitu} for the different study areas (N is the number of collocations).

Cases study	Statistic indicator	SSS_{SMOS}	$SSS_{SMOS\ A+T}$	SSS_{TOPAZ}
Beaufort Sea	MoD (pss)	−2.12	−0.83	3.67
	STDD (pss)	0.96	0.88	1.18
	r	0.86	0.88	0.86
	N	3912	3912	3912
Chukchi Sea	MoD (pss)	−1.50	−1.28	1.97
	STDD (pss)	1.47	1.23	1.78
	r	0.84	0.88	0.86
	N	90,721	90,721	90,721
Laptev Sea	MoD (pss)	−1.97	0.11	1.51
	STDD (pss)	1.82	1.17	1.89
	r	0.53	0.75	0.04
	N	4048	4048	4048
Barents Sea	MoD (pss)	−1.59	−0.17	−0.19
	STDD (pss)	0.96	0.94	0.50
	r	−0.03	−0.04	0.19
	N	10,879	10,879	10,879
Atlantic Area	MoD (pss)	−1.29	−0.51	0.01
	STDD (pss)	1.02	1.13	0.10
	r	0.01	−0.05	0.70
	N	2876	2876	2876
Arctic Ocean	MoD (pss)	−1.54	−0.27	1.25
	STDD (pss)	1.46	1.28	1.86
	r	0.92	0.94	0.89
	N	156,986	156,986	156,986

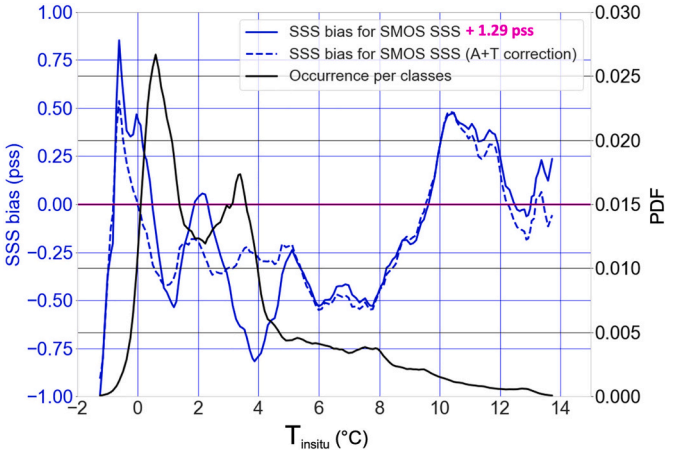

Fig. 12. Averaged differences between SSS_{SMOS} + 1.29pss (in order to consider the general bias) or $SSS_{SMOS\ A+T}$ and S_{insitu} and PDF of collocations per bin of in-situ SST; (bin size: 1 °C – sliding window).

Table 3
MoD, STDD and r between $SSS_{SMOS\ A+T}$ or TOPAZ SSS and in-situ measurements for the underway TSG case studies.

Cases study	Statistic indicator	$SSS_{SMOS\ A+T}$	SSS_{TOPAZ}
Case study 1	MoD (pss)	1.25	1.41
	STDD (pss)	1.27	1.43
	r	0.88	0.96
Case study 2	MoD (pss)	0.59	0.25
	STDD (pss)	1.37	0.98
	r	0.84	0.69
Case study 3	MoD (pss)	−0.15	0.51
	STDD (pss)	1.24	1.43
	r	0.56	0.12

and T_{insitu}. The correction strongly improves the SMOS SSS estimate. This relies on the importance of correcting prior SST in cold regions where the sensitivity of TB to SSS is low. The effect of the SST correction is particularly noticeable in the Arctic Seas where river inflows generate strong SST gradients associated with strong SSS gradients: after this SST correction the SSS variability becomes much closer to the observations (Fig. 14a).

Our correction makes use of SST_{REMSS} obtained by merging microwave and IR SST. The use of the REMSS "microwave only" OI SST gives very close statistical results (Appendix-F). Nevertheless, statistics obtained with SST_{REMSS} "microwave only" are slightly better for two reasons: 1/ the sea ice filtering of SST_{REMSS} "microwave only" is more stringent than the one of SST_{REMSS} and, in some cases, than the one based on SMOS Acard; 2/ SST_{REMSS} "microwave only" are not provided too close from the coast where SSS uncertainty is higher.

Our correction does not reveal the complexity of biases resulting from land/sea contrast, but land/sea bias correction in the Arctic Ocean is a challenging issue that needs to be investigated in further studies. It is likely one of the reasons why SSS calibration needs to be adjusted. Another limitation of the correction methodology is that we only consider issues with SST and dielectric constant model: surface roughness effects linked to e.g. wind in limited fetch areas or to surfactants could also play a role, but these effects were out of the scope of our study.

The quality of our new product is assessed by comparison with various in-situ measurements (Argo, Underway TSG and CTD casts) and with an ocean model outputs (TOPAZ). In-situ measurements cover a large range of SSS. The in-situ salinity measurement depth (between 1 m and 10 m) is shown to have a strong impact on the difference between SSS_{SMOS} and S_{insitu}, especially in low SSS areas (e.g., rivers plumes) that are often very stratified in salinity close to the surface. Hence only S_{insitu} between 1 m and 5 m depth are retained for the validation.

The corrected SSS better performs than TOPAZ reanalysis, essentially in areas of large temporal and spatial variability. Over the whole Arctic Ocean, STDD between weekly corrected SMOS SSS and S_{insitu} is of 1.28 pss, while STDD between TOPAZ SSS and S_{insitu} is of 1.86 pss. The statistics of the comparisons with S_{insitu} in the various regions (the Beaufort, Chukchi, Laptev and Barents Seas, and an Atlantic Area) are more stable from one study area to another with corrected SMOS SSS than with TOPAZ SSS. SMOS STDD vary between 0.94 pss and 1.23 pss, while TOPAZ STDD vary between 0.50 pss and 1.89 pss. The mean differences obtained with SMOS SSS vary between −1.28 pss and 0.11 pss while the ones obtained with TOPAZ SSS vary between −0.19 pss and 3.67 pss. SMOS SSS captures high variability in fresh Arctic Seas with a favorable signal to noise ratio as shown by high correlation levels on the order of 0.8 between SMOS SSS and in-situ S_{insitu}. It is not the case in less variable salty Arctic Seas (Table 2).

While collocations with in-situ measurements, in particular underway TSG from research vessel, demonstrates SMOS ability to capture SSS (temporal and spatial) variability at short scale, SMOS SSS seasonal averages bring a new perspective on the SSS variability in the Arctic Ocean. Compared with the TOPAZ reanalysis, it shows a larger variability in river plumes and differences of pattern, e.g. in the Beaufort gyre (Figs. 15 and 16). These observations suggest complementarity between SMOS SSS and TOPAZ reanalysis products. This was already demonstrated by Xie et al. (2019) for Arctic SSS produced at the Barcelona Expert center, but this is even more evident with this new product in very variable Arctic Seas (Appendix-H, Laptev Sea and Beaufort Sea).

The presented SSS product demonstrates valuable performances compared to other SSS products in Arctic Ocean (Appendix-H). It provides avenues for improvement in the ESA L2 OS processor concerning

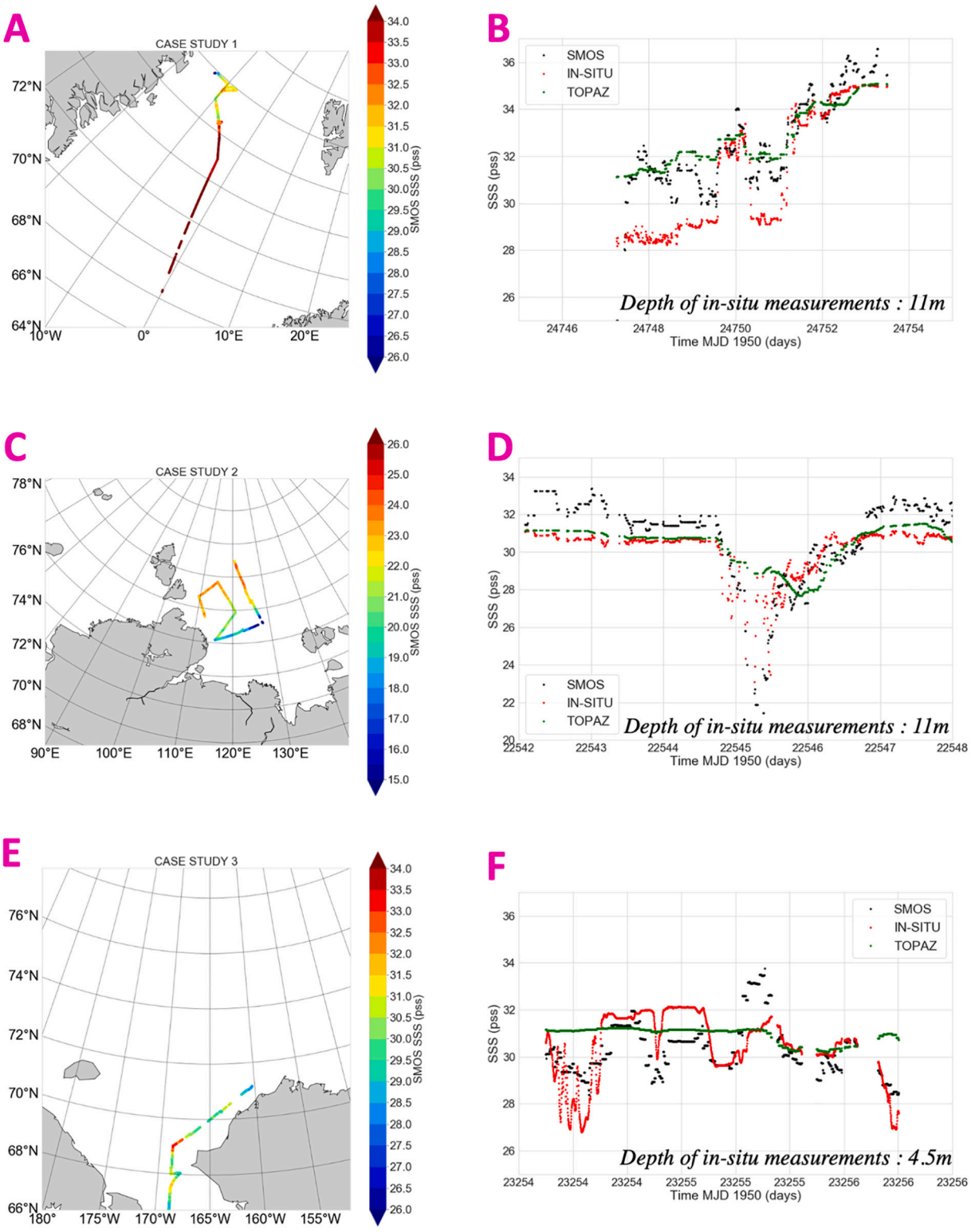

Fig. 13. (A, C, E) SMOS SSS measurements collocated with underway TSG measurements; (B, D, F) Time series of SMOS SSS (black) and TOPAZ SSS (green) collocated with underway TSG salinity measurements (red). Case studies in the Greenland Sea (A, D, G), in the Laptev Sea (B, E, H) and Chukchi Sea (C, F, I).

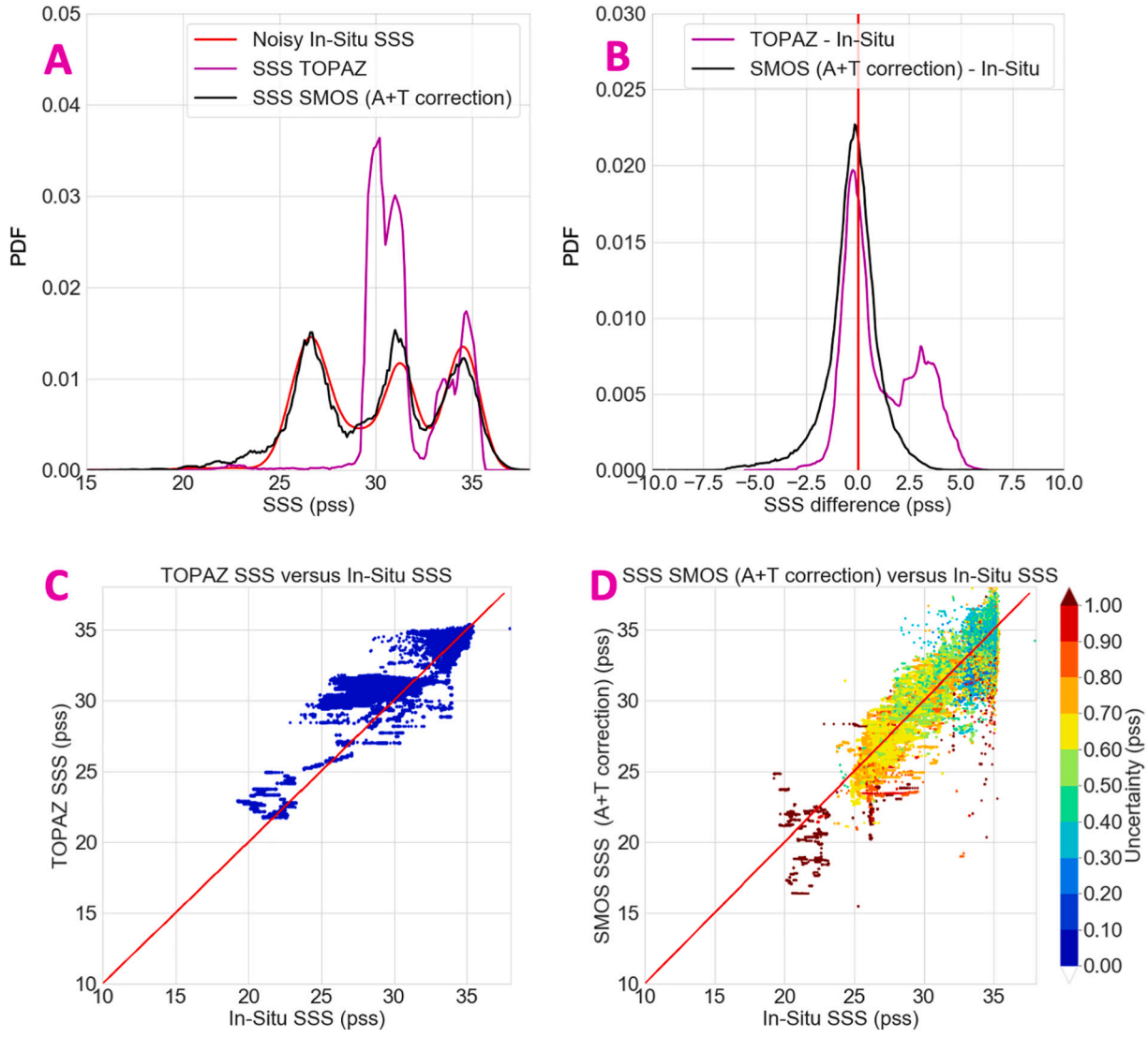

Fig. 14. (A) Distribution of SSS for TOPAZ (magenta), SMOS (black) and S_{insitu} (red) (B) Distribution of errors between SMOS SSS and S_{insitu} (black) and TOPAZ SSS and S_{insitu} (magenta) (C) Scatterplot of TOPAZ SSS versus S_{insitu}; (D) Scatterplot of SMOS SSS versus S_{insitu} with SMOS theoretical uncertainty coded in colour. (For interpretation of the references to colour in this figure legend, the reader is referred to the web version of this article.)

the detection of sea ice, the correction of dielectric constant and SST related flaws. Moreover, additional work is needed in areas with lower SSS variability and RFI contamination as in the North Atlantic. In addition to the methods presented in this study, a correction for the land/sea contamination and the latitudinal biases as presented by Boutin et al. (2018) or/and an optimal interpolation using complementarity between SMOS SSS and in-situ measurements could further improve SSS derived from SMOS mission in the Arctic Ocean.

This study highlights the importance of sea ice filtering. In that respect, increasing the spatial resolution of L-band interferometric radiometer measurements to 10 km, as proposed by the SMOS-HR project (Rodríguez-Fernández et al., 2019), would greatly help to better filter the ocean areas partially covered by sea ice and would allow to get closer to the ice edge and to land.

This study highlights the importance of using an SST prior consistent with L-Band radiometric measurement for SSS retrieval in the Arctic Ocean. Ideally, the prior SST should be measured at the same spatial resolution and at the same time as the L-band measurement. One of the major CIMR (Copernicus Image Microwave Radiometer, Kilic et al., 2018) mission goal over the ocean is to provide simultaneous SSS and SST measurements but at different spatial resolution (SSS from the L-Band TB at ~60 km resolution and SST from the C/X-band channels at ~15 km). Joined and simultaneous SSS/SST estimates at the same resolution than the L-Band channel, i.e., 36×60 km^2 will therefore be available from this sensor but at a rather low spatial resolution for the estimate of the SSS field. Complementarily, SMOS-HR interferometric mission goal is to provide L-Band TB and therefore SSS at a spatial resolution (~10 km) close to CIMR SST resolution but it won't include an independent SST sensor. Hence combining measurements from both missions would very likely improve SSS fields estimates in the Arctic Ocean.

This study is limited to the analysis of SSS provided by the SMOS satellite mission in the Arctic Ocean. Nevertheless, during the period considered in this study, two other satellite missions, SMAP and

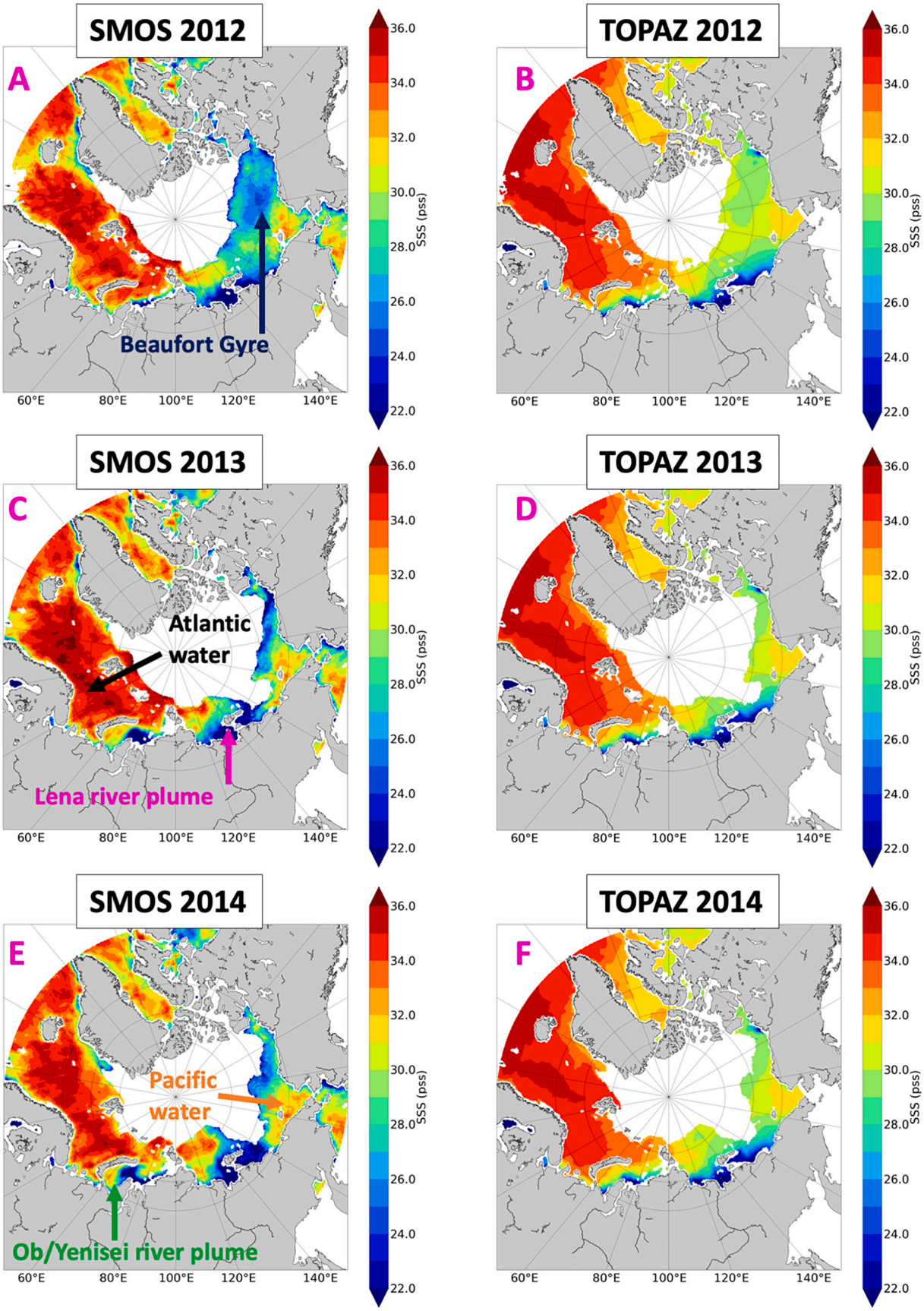

Fig. 15. SSS average for the period from August to October for year 2012, 2013 and 2014; (left column) $SSS_{SMOS\ A+T}$; (right column) SSS_{TOPAZ}.

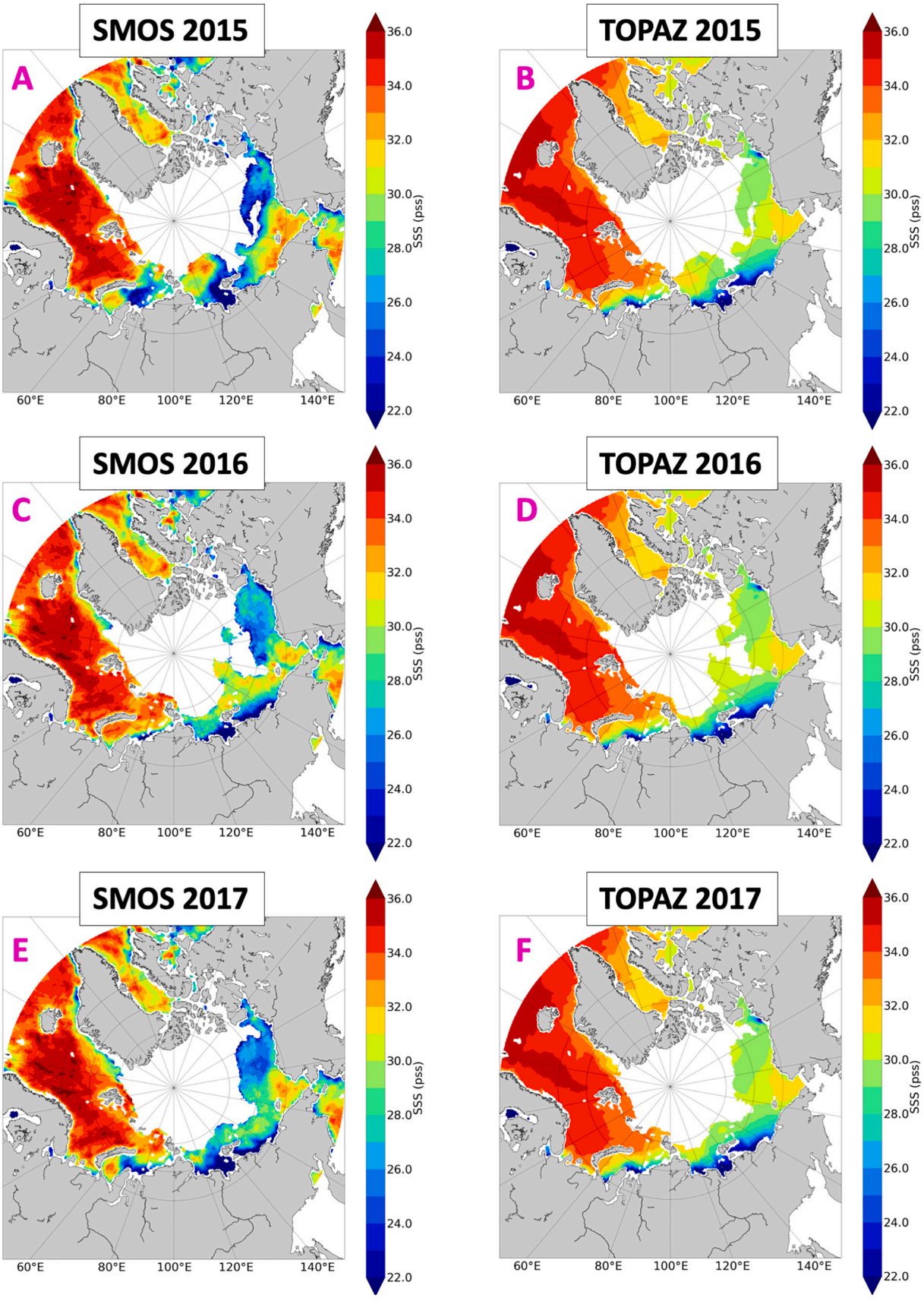

Fig. 16. SSS average from August to October for year 2015, 2016 and 2017; (left column) $SSS_{SMOS\ A+T}$; (right column) SSS_{TOPAZ}.

Aquarius, have monitored SSS over the global ocean. The CCI + SSS project run as a part of ESA Climate Change Initiative aims at generating improved and consistent multi-satellites SSS fields and should bring a decisive improvement to the level 4 SSS maps, especially in the Arctic Ocean due to the short revisit time allowed by the orbit configuration of these satellites. The avenue for SMOS processing improvement that we propose should also benefit to the CCI + SSS products that incorporate SMOS measurements.

Declaration of Competing Interest

The authors declare that they have no known competing financial interests or personal relationships that could have appeared to influence the work reported in this paper.

Acknowledgments

AS is supported by a SU Ph. D. grant. This work was supported by CNES-TOSCA 'SMOS-Ocean', CNES Centre Aval de Traitement des Données SMOS (CATDS) and ESA 'Expert Support Laboratory for level 2 Ocean Salinity' projects. AT acknowledges financial support from the Ministry of Science and Higher Education of the Russian Federation, project RFMEFI61617X0076.

Appendix A. Acard retrieval in the SMOS level 2 processor

As shown by Waldteufel et al. (2004), simultaneous retrieval of the real, e', and imaginary part, e", of dielectric constant from SMOS TB is an ill posed problem as the cost function, rather than a single minimum, exhibits a minimum valley, that can be represented analytically using a modified cardioid model. After carrying out the following change of variable:

$$e' = Acard\,(1 + \cos(Ucard))\cos(Ucard) + Bcard$$

$$e'' = Acard\,(1 + \cos(Ucard))\sin(Ucard) \quad (A1)$$

which is equivalent to:

$$Acard = mcard^2/(mcard + e' - Bcard)$$

$$Ucard = \tan^{-1}(e''/(e' - Bcard))$$

$$with: mcard = ((e' - Bcard)^2 + e''^2)^{1/2} \quad (A2)$$

Bcard corresponds to the observed offset between the observed modified cardioid and the true analytical formulation for a cardioid model. With Bcard = 0.8 (optimal value that minimizes the retrieval error on Acard), it is possible to retrieve the parameter Acard with good accuracy: a minimum of χ^2 is seen as a vertical line corresponding to a constant value of Acard and various values of Ucard. Local minima of χ^2 are also observed for unrealistic negative values of Acard; as it will be described in the following, retrieval of such negative values are avoided by taking an error on prior Acard over the ocean of 20 units or by initiating the retrieval with low Acard value as low card are much better constrained.

It is clear that the minimization of χ^2 parameter does not allow to retrieve a single pair of (e', e") while it allows to retrieve a single value of Acard, Ucard remaining undetermined.

We found that initiating the retrieval with low Acard prior value ($Acard^{prior} = 1$) and large error on Acard ($s_{A\_card} = 50$) allows to avoid retrieval of negative Acard values while avoiding biases on low Acard values and gives the same result over ocean pixels as taking $Acard^{prior}$ deduced from mean SSS and SST.

The ESA L2 Ocean Salinity processor retrieves Acard from SMOS Tb corrected from the roughness model plus atmospheric and galactic noise corrections.

Appendix B. HEINCKE and POLARSTERN cruise track datasets used in this study.

HEINCKE cruise track HE493	https://doi.pangaea.de/10.1594/PANGAEA.887938
HEINCKE cruise track HE387	https://doi.pangaea.de/10.1594/PANGAEA.859752
HEINCKE cruise track HE492	https://doi.pangaea.de/10.1594/PANGAEA.887937
HEINCKE cruise track HE333	https://doi.pangaea.de/10.1594/PANGAEA.859705
HEINCKE cruise track HE451–1	https://doi.pangaea.de/10.1594/PANGAEA.863418
HEINCKE cruise track HE449	https://doi.pangaea.de/10.1594/PANGAEA.863416
HEINCKE cruise track HE408	https://doi.pangaea.de/10.1594/PANGAEA.859774
HEINCKE cruise track HE450	https://doi.pangaea.de/10.1594/PANGAEA.863417
POLARSTERN cruise track ARK-XXVI/2	https://doi.pangaea.de/10.1594/PANGAEA.770035
POLARSTERN cruise track PS109	https://doi.pangaea.de/10.1594/PANGAEA.889548
POLARSTERN cruise track PS93.2	https://doi.pangaea.de/10.1594/PANGAEA.863229
POLARSTERN cruise track ARK-XXVII/1	https://doi.pangaea.de/10.1594/PANGAEA.802811
POLARSTERN cruise track PS99.1	https://doi.pangaea.de/10.1594/PANGAEA.873156
POLARSTERN cruise track PS92	https://doi.pangaea.de/10.1594/PANGAEA.863234
POLARSTERN cruise track ARK-XXVII/3	https://doi.pangaea.de/10.1594/PANGAEA.808835
POLARSTERN cruise track ARK-XXVI/1	https://doi.pangaea.de/10.1594/PANGAEA.770034
POLARSTERN cruise track ARK-XXVI/3	https://doi.pangaea.de/10.1594/PANGAEA.770828
POLARSTERN cruise track ARK-XXVII/2	https://doi.pangaea.de/10.1594/PANGAEA.802812
POLARSTERN cruise track PS107	https://doi.pangaea.de/10.1594/PANGAEA.889535
POLARSTERN cruise track PS100	https://doi.pangaea.de/10.1594/PANGAEA.873158
POLARSTERN cruise track PS93.1	https://doi.pangaea.de/10.1594/PANGAEA.863228
POLARSTERN cruise track PS101	https://doi.pangaea.de/10.1594/PANGAEA.873145
POLARSTERN cruise track PS99.2	https://doi.pangaea.de/10.1594/PANGAEA.873153
POLARSTERN cruise track PS86	https://doi.pangaea.de/10.1594/PANGAEA.858880

Appendix C. Difference of repartition of in-situ measurements used in this study between 1-m and 3-m and between 1-m and 5-m

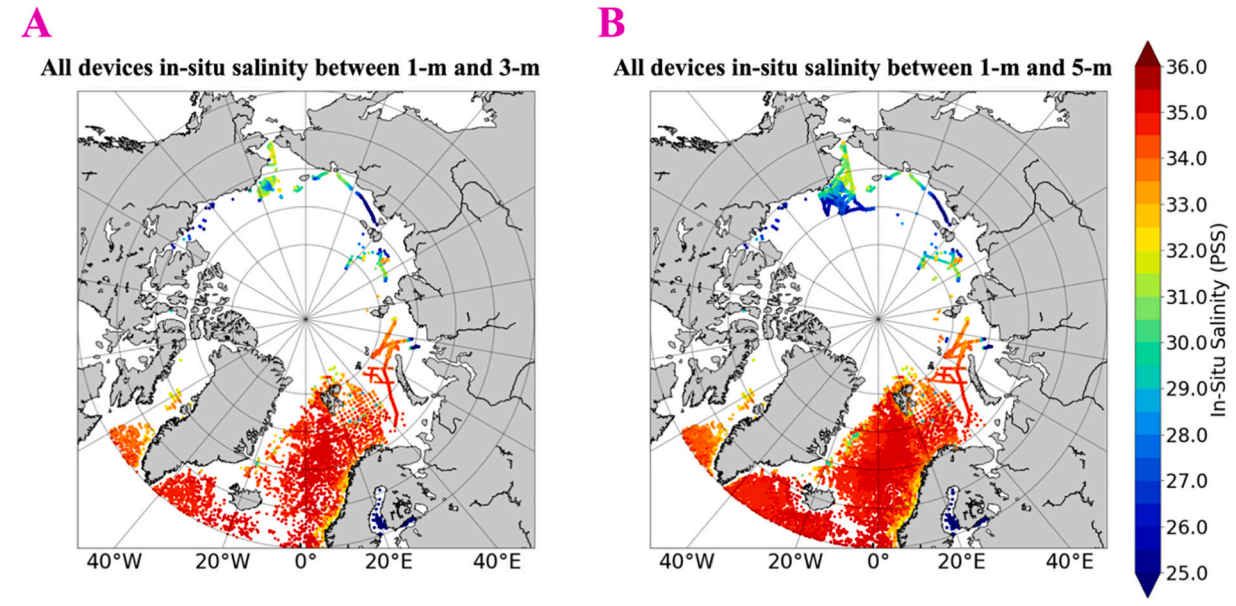

Fig. C1. SSS of in-situ measurements used in the study (A) between 1-m and 3-m depth; (B) between 1-m and 5-m depth.

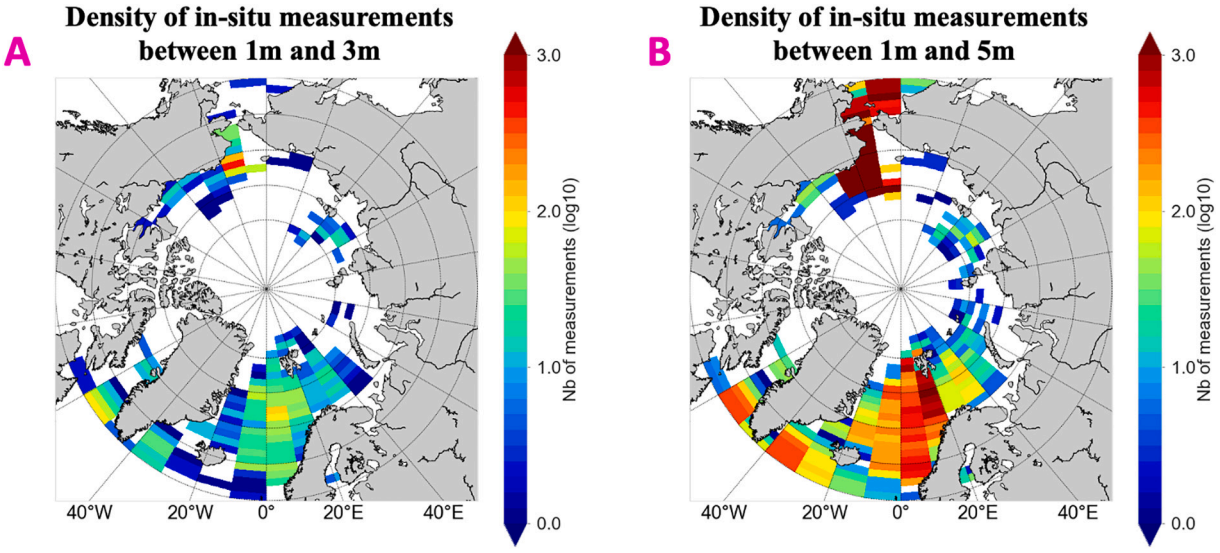

Fig. C2. Density of in-situ measurements used in the study (A) between 1-m and 3-m depth; (B) between 1-m and 5-m depth.

Appendix D. Example of differences recorded between SST from OSTIA and SST_{REMSS}.

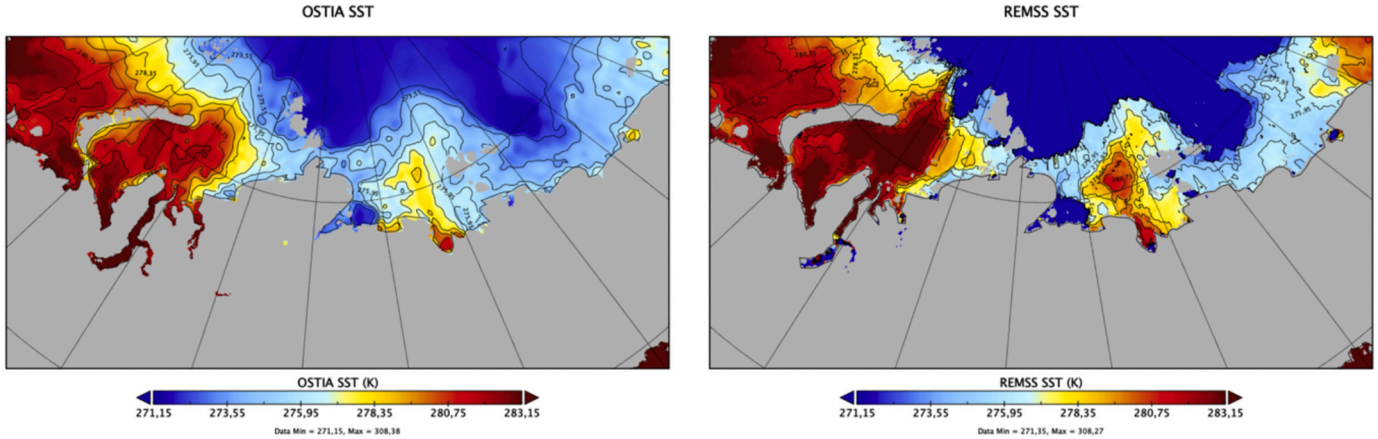

Fig. D1. Analyzed SST for 2015/08/15 from (Left) OSTIA; (Right) REMSS (MW + IR).

Appendix E. MoD, STDD and r between different versions of SMOS SSS and $S_{in\text{-}situ}$ for the different study areas. The number of collocations is equivalent to the Table 1.

Cases study	Statistic indicator	SSS_{SMOS}	$SSS_{SMOS\ A}$	$SSS_{SMOS\ T}$	$SSS_{SMOS\ A+T}$
Beaufort Sea	MoD (pss)	−2.12	−1.44	−1.51	−0.83
	STDD (pss)	0.96	0.98	1.08	0.88
	r	0.86	0.83	0.83	0.88
Chukchi Sea	MoD (pss)	−1.50	−1.28	−0.49	−0.28
	STDD (pss)	1.47	1.60	1.18	1.23
	r	0.84	0.81	0.89	0.86
Laptev Sea	MoD (pss)	−1.97	−1.39	−0.43	0.12
	STDD (pss)	1.82	2.16	1.07	1.17
	r	0.53	0.40	0.80	0.75
Barents Sea	MoD (pss)	−1.59	−0.24	−1.49	−0.17
	STDD (pss)	0.96	0.97	0.94	0.94
	r	−0.03	−0.02	−0.05	−0.02
Atlantic Area	MoD (pss)	−1.29	−0.55	−1.25	−0.51
	STDD (pss)	1.02	1.15	1.00	1.13
	r	0.01	−0.05	0.02	−0.05
Arctic Ocean	MoD (pss)	−1.54	−0.77	−0.99	−0.27
	STDD (pss)	1.46	1.60	1.32	1.28
	r	0.92	0.92	0.93	0.94

Appendix F. MoD, STDD, r and N (number of collocations) between different versions of SMOS SSS or TOPAZ SSS and in-situ measurements for the different study areas (with $SSS_{SMOS\ A+T}$ derived using SST_{REMSS} in black and $SSS_{SMOS\ A+T}$ derived using $SST_{REMSS\ MWO}$ in bold black – collocations are not exactly the same due to a difference of sea ice mask between SST_{REMSS} and $SST_{REMSS\ MWO}$, and a difference of coverage close from coast – colocations with in-situ measurements are the same between SSS_{SMOS}, $SSS_{SMOS\ A+T}$ and SSS_{TOPAZ}).

Cases study	Statistic indicator	SSS_{SMOS}	$SSS_{SMOS\ A+T}$	SSS_{TOPAZ}
Beaufort Sea	MoD (pss)	−2.25	−0.98	3.99
		−2.25	**−0.96**	**3.99**
	STDD (pss)	0.94	0.83	1.07
		0.94	**0.87**	**1.07**
	r	0.81	0.84	0.81
		0.81	**0.84**	**0.81**
	N	3128	3128	3128
		3128	**3128**	**3128**
Chukchi Sea	MoD (pss)	−1.39	−0.21	1.94
		−1.39	**−0.27**	**1.94**
	STDD (pss)	1.30	1.08	1.79
		1.30	**1.07**	**1.79**
	r	0.86	0.91	0.87
		0.86	**0.90**	**0.87**
	N	86,917	86,917	86,917
		86,917	**86,917**	**86,917**
Laptev Sea	MoD (pss)	−2.45	−0.17	0.82
		−2.45	**−0.19**	**0.82**
	STDD (pss)	1.69	1.03	1.46
		1.69	**1.01**	**1.46**
	r	0.61	0.74	0.32
		0.61	**0.75**	**0.32**
	N	3190	3190	3190
		3190	**3190**	**3190**
Barents Sea	MoD (pss)	−1.58	−0.16	−0.20
		−1.58	**−0.15**	**−0.20**
	STDD (pss)	0.95	0.93	0.49
		0.95	**0.93**	**0.49**
	r	−0.07	−0.05	0.19
		−0.07	**−0.05**	**0.19**
	N	10,762	10,762	10,762
		10,762	**10,762**	**10,762**
Atlantic area	MoD (pss)	−1.28	−0.50	0.01
		−1.28	**−0.49**	**0.01**
	STDD (pss)	0.99	1.10	0.10
		0.99	**1.09**	**0.10**
	r	0.02	−0.04	0.70
		0.02	**−0.04**	**0.70**
	N	2865	2865	2865
		2865	**2865**	**2865**

Arctic Ocean	MoD (pss)	−1.46	−0.21	1.20
		−1.46	**−0.25**	**1.20**
	STDD (pss)	1.31	1.15	1.86
		1.31	**1.15**	**1.86**
	r	0.93	0.95	0.89
		0.93	**0.95**	**0.89**
	N	148,655	148,655	148,655
		148,655	**148,655**	**148,655**

Appendix G. Example of differences recorded between $SSS_{SMOS\ A+T}$ using SST_{REMSS} or using $SST_{REMSS\ MWO}$ in comparison of differences between SSS_{SMOS} and $SSS_{SMOS\ A+T}$ (using SST_{REMSS}).

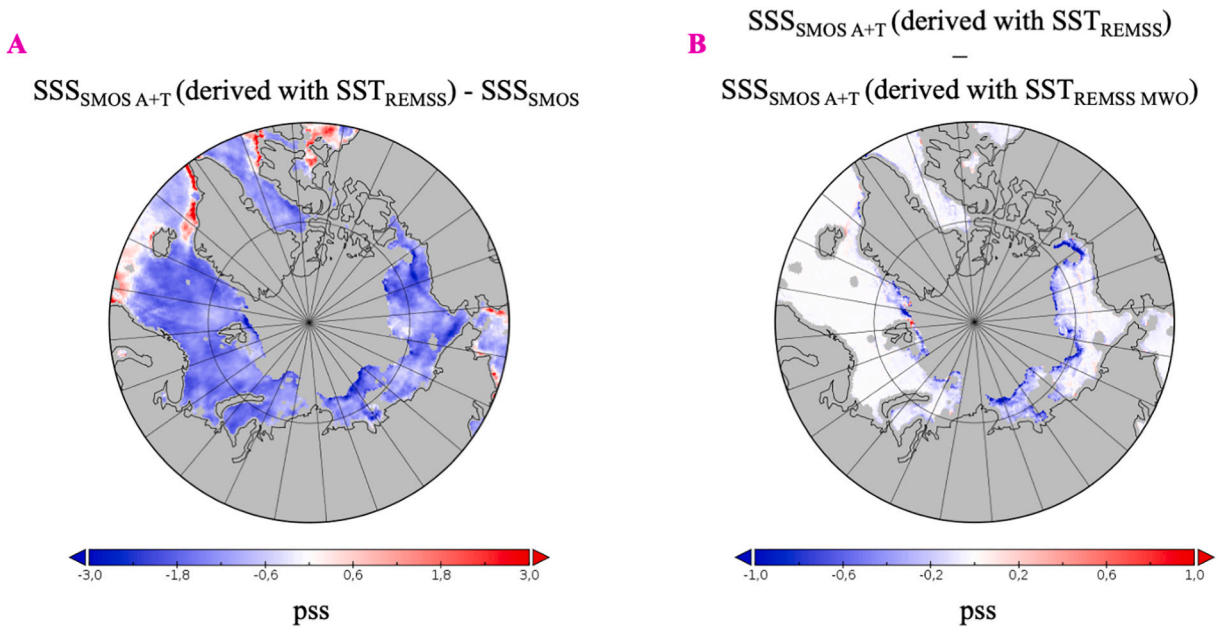

Fig. G1. (A) difference between SSS_{SMOS} and $SSS_{SMOS\ A+T}$ (computed using SST_{REMSS}) average for the period from August to October 2017; (B) difference between $SSS_{SMOS\ A+T}$ (computed using SST_{REMSS}) and $SSS_{SMOS\ A+T}$ (computed using $SST_{REMSS\ MWO}$) average for the period from August to October 2017.

Appendix H. MoD, STDD, r and N (number of collocations) between different versions of SMOS SSS or TOPAZ SSS and in-situ measurements for the different study areas. In SSS SMOS column, first line : ice filtered SMOS SSS , second line : SMOS BEC v2 (Olmedo et al., 2018) and third line : SMOS CEC v3 (Boutin et al., 2018).

Cases study	Statistic indicator	SSS_{SMOS}	$SSS_{SMOS\ A+T}$	SSS_{TOPAZ}
Beaufort Sea	MoD (pss)	−2.12 (1.04) (3.51)	−0.83	3.67
	STDD (pss)	0.96 (1.85) (2.35)	0.88	1.18
	r	0.86 (0.78) (0.76)	0.88	0.86
	N	(3912) (3976) (4434)	3912	3912
Chukchi Sea	MoD (pss)	−1.50 (0.53) (3.00)	−1.28	1.97
	STDD (pss)	1.47 (1.48) (1.87)	1.23	1.78
	r	0.84 (0.83) (0.54)	0.88	0.86
	N	(90,721) (100908) (105986)	90,721	90,721

Laptev Sea	MoD (pss)	−1.97 (0.37) (0.59)	0.11	1.51
	STDD (pss)	1.82 (1.85) (2.35)	1.17	1.89
	r	0.53 (0.39) (−0.10)	0.75	0.04
	N	(4048) (3391) (3391)	4048	4048
Barents Sea	MoD (pss)	−1.59 (−0.01) (0.35)	−0.17	−0.19
	STDD (pss)	0.96 (0.88) (1.39)	0.94	0.50
	N	(10,879) (15571) (18622)	10,879	10,879
	r	−0.03 (0.31) (−0.14)	−0.04	0.19
Atlantic Area	MoD (pss)	−1.29 (0.01) (0.01)	−0.51	0.01
	STDD (pss)	1.02 (0.27) (0.66)	1.13	0.10
	r	0.01 (0.38) (−0.05)	−0.05	0.70
	N	(2876) (5863) (6168)	2876	2876
Arctic Ocean	MoD (pss)	−1.54 (0.12) (1.55)	−0.27	1.25
	STDD (pss)	1.46 (1.65) (2.30)	1.28	1.86
	r	0.92 (0.93) (0.86)	0.94	0.89
	N	(156986) (196665) (225904)	156,986	156,986

References

Björk, G., 2017. CTD Data from the SWERUS-C3 Expedition 2014 in the Arctic Ocean. PANGAEAhttps://doi.org/10.1594/PANGAEA.884144.

Boutin, J., Chao, Y., Asher, W.E., Delcroix, T., Drucker, R., Drushka, K., Kolodziejczyk, N., Lee, T., Reul, N., Reverdin, G., Schanze, J., Soloviev, A., Yu, L., Anderson, J., Brucker, L., Dinnat, E., Santos-Garcia, A., Jones, W.L., Maes, C., Meissner, T., Tang, W., Vinogradova, N., Ward, B., 2016. Satellite and in situ salinity: understanding near-surface stratification and subfootprint variability. Bull. Amer. Meteor. Soc. 97, 1391–1407. https://doi.org/10.1175/BAMS-D-15-00032.1.

Boutin, J., Vergely, J.L., Marchand, S., D'Amico, F., Hasson, A., Kolodziejczyk, N., Reul, N., Reverdin, G., Vialard, J., 2018. New SMOS sea surface salinity with reduced systematic errors and improved variability. Remote Sens. Environ. 214, 115–134. https://doi.org/10.1016/j.rse.2018.05.022.

Brucker, L., Dinnat, E.P., Koenig, L.S., 2014. Weekly gridded Aquarius L-band radiometer/scatterometer observations and salinity retrievals over the polar regions, Part 2: Initial product analysis. The Cryosphere 8 (3), 915–930. https://www.the-cryosphere.net/8/915/2014/ https://doi.org/10.5194/tc-8-915-2014.

Carmack, E.C., 2007. The alpha/beta ocean distinction: a perspective on freshwater fluxes, convection, nutrients and productivity in high-latitude seas. Deep Sea Res. Part II Top. Stud. Oceanogr. 54, 3–26. https://doi.org/10.1016/j.dsr2.2007.08.018. Pages 2578-2598, ISSN 0967-0645.

Carmack, E.C., et al., 2016. Freshwater and its role in the Arctic marine system : sources, disposition, storage, export, and physical and biogeochemical consequences in the Arctic and global oceans. J. Geophys. Res. Biogeosci. 121, 675–717. https://doi.org/10.1002/2015JG003140.

Chassignet, E.P., Hurlburt, H.E., Metzger, E.J., Smedstad, O.M., Cummings, J.A., Halliwell, G.R., Bleck, R., Baraille, R., Wallcraft, A.J., Lozano, C., Tolman, H.L., Srinivasan, A., Hankin, S., Cornillon, P., Weisberg, R., Barth, A., He, R., Werner, F., Wilkin, J., 2009. US GODAE: global Ocean prediction with the HYbrid coordinate ocean model (HYCOM). Oceanography 22 (2), 64–75. https://doi.org/10.5670/oceanog.2009.39.

Dinnat, E.P., Le Vine, D.M., Boutin, J., Meissner, T., Lagerloef, G., 2019. Remote Sensing, 2072–4292, 11, 7, 750, Remote Sensing of Sea Surface Salinity: Comparison of Satellite and in Situ Observations and Impact of Retrieval Parameters. https://doi.org/10.3390/rs11070750. https://www.mdpi.com/2072-4292/11/7/750.

Donlon, C.J., Martin, M., Stark, J., Roberts-Jones, J., Fiedler, E., Wimmer, W., 2012. The operational sea surface temperature and sea ice analysis (OSTIA) system. Remote Sens. Environ. 116, 140–158. https://doi.org/10.1016/j.rse.2010.10.017.

ECMWF, 2016. IFS Documentation CY41R2. Part II : Data Assimilation. IFS Documentation. ECMWF.

Font, J., Camps, A., Borges, A., Martin-Neira, M., Boutin, J., Reul, N., Kerr, Y.H., Hahne, A., Mecklenburg, S., 2010. SMOS: the Challenging Sea surface salinity measurement from space. Proc. IEEE 98 (5), 649–665. https://doi.org/10.1109/jproc.2009.2033096.

Haine, T.W., Curry, B., Gerdes, R., Hansen, E., Karcher, M., Lee, C., Rudels, B., Spreen, G., de Steur, L., Stewart, K.D., Woodgate, R., 2015. Arctic freshwater export: status, mechanisms, and prospects. Glob. Planet. Chang. 125, 13–35. https://doi.org/10.1016/j.gloplacha.2014.11.013.

Høyer, J.L., Karagali, I., Dybkjær, G., Tonboe, R., 2012. Multi sensor validation and error characteristics of Arctic satellite sea surface temperature observations. In: Remote Sensing of Environment, Volume 121, pp. 335–346. ISSN 0034-4257. https://doi.org/10.1016/j.rse.2012.01.013.

IPCC, 2018. Summary for Policymakers. In: Masson-Delmotte, V., Zhai, P., Pörtner, H.O., Roberts, D., Skea, J., Shukla, P.R. ... Waterfield, T. (Eds.), Global warming of 1.5°C. An IPCC Special Report on the impacts of global warming of 1.5°C above pre-industrial levels and related global greenhouse gas emission pathways, in the context of strengthening the global response to the threat of climate change, sustainable development, and efforts to eradicate poverty. World Meteorological Organization, Geneva, Switzerland 32 pp.

Ivanov, V., et al., 2013. NABOS 2013 Arctic Expedition aboard RV "Akademik Fedorov".

https://nabos.iarc.uaf.edu/NABOS2/data/registered/2013/metadata/brief_report_2013-engl.pdf.
JAMSTEC, 2013a. MIRAI MR12-E03 Cruise Data. JAMSTEC. https://doi.org/10.17596/0001847. (accessed 2019-07-16).
JAMSTEC, 2013b. MIRAI MR13–06 Leg1 Cruise Data. JAMSTEC. https://doi.org/10.17596/0001856. (accessed 2019-07-16).
JAMSTEC, 2015. MIRAI MR14–05 Cruise Data. JAMSTEC. https://doi.org/10.17596/0001861. (accessed 2019-07-16).
Kerr, Y.H., et al., 2010. The SMOS Mission : new tool for monitoring key elements of the global water cycle. Proc. IEEE 98 (5), 666–687.
Kilic, L., Prigent, C., Aires, F., Boutin, J., Heygster, G., Tonboe, R.T., et al., 2018. Expected performances of the Copernicus imaging microwave radiometer (CIMR) for an all-weather and high spatial resolution estimation of ocean and sea ice parameters. J. Geophys. Res. Oceans 123, 7564–7580. https://doi.org/10.1029/2018JC014408.
Klein, L.A., Swift, C.T., 1977. An improved model for the dielectric constant of sea water at microwave frequencies. IEEE J. Ocean. Eng. 2, 104–111. https://doi.org/10.1109/JOE.1977.1145319.
Köhler, J., Sena Martins, M., Serra, N., Stammer, D., 2015. Quality assessment of spaceborne sea surface salinity observations over the northern North Atlantic. J. Geophys. Res. Oceans 120, 94–112. https://doi.org/10.1002/2014JC010067.
Lagerloef, G., et al., 2008. The aquarius/SAC-D mission: designed to meet the salinity remote sensing challenge. Oceanography 21 (1), 68–81.
Lind, S., Ingvaldsen, R.B., Furevik, T., 2018. Arctic warming hotspot in the northern Barents Sea linked to declining sea-ice import. Nat. Clim. Chang. https://doi.org/10.1038/s41558-018-0205-y.
Makhotin, M., Ivanov, V., 2018a. Physical Oceanography Measured with CTD/Watersampler-System During PU2012 to the Barents Sea in 2012. PANGAEAhttps://doi.org/10.1594/PANGAEA.895269.
Makhotin, M., Ivanov, V., 2018b. physical Oceanography Measured with ctd/water-sampler-System During pu2013 to the Barents Sea in 2013. PANGAEA.
Makhotin, M., Ivanov, V., 2018c. Physical Oceanography Measured with CTD/Watersampler-System during PU2014 to the Barents Sea in 2014. PANGAEAhttps://doi.org/10.1594/PANGAEA.895271.
Matsuoka, A., Babin, M., Devred, E.C., 2016. A new algorithm for discriminating water sources from space: a case study for the southern Beaufort Sea using MODIS Ocean color and SMOS salinity data. Remote Sens. Environ. 184, 124–138. ISSN 0034-4257. https://doi.org/10.1016/j.rse.2016.05.006.
Meissner, T., Wentz, F.J., Scott, J., Vazquez-Cuervo, J., 2016. Sensitivity of ocean surface salinity measurements from Spaceborne L-band radiometers to Ancillary Sea surface temperature. IEEE Trans. Geosci. Remote Sens. 54 (12), 7105–7111. https://doi.org/10.1109/TGRS.2016.2596100.
Olmedo, E., Gabarró, C., González-Gambau, V., Martínez, J., Ballabrera-Poy, J., Turiel, A., Portabella, M., Fournier, S., Lee, T., 2018. Seven years of SMOS Sea surface salinity at high latitudes: variability in Arctic and sub-Arctic regions. Remote Sens. 10, 1772. https://doi.org/10.3390/rs10111772.
Peralta-Ferriz, C., Woodgate, R.A., 2015. Seasonal and interannual variability of pan-Arctic surface mixed layer properties from 1979 to 2012 from hydrographic data, and the dominance of stratification for multiyear mixed layer depth shoaling. Prog. Oceanogr. 134, 19–53. ISSN 0079-6611. doi.10.1016/j.pocean.2014.12.005.
Piepmeier, J.R., et al., 2017. SMAP L-band microwave radiometer : instrument design and first year on orbit. IEEE Trans. Geosci. Remote Sens. 55 (4), 1954–1966. https://doi.org/10.1109/TGRS.2016.2631978.
Polyakov, I., Ashik, I., Ivanov, V., 2015. IARC Technical Report #9 Report of the NABOS 2015 Expedition Activities in the Arctic Ocean. https://nabos.iarc.uaf.edu/NABOS2/data/registered/2015/metadata/Report_2015.pdf.
Reul, N., Grodsky, S.A., Arias, M., Boutin, J., Catany, R., Chapron, B., D'Amico, F., Dinnat, E., Donlon, C., Fore, A., Fournier, S., Guimbard, S., Hasson, A., Kolodziejczyk, N., Lagerloef, G., Lee, T., Le Vine, D.M., Lindstrom, E., Maes, C., Mecklenburg, S., Meissner, T., Olmedo, E., Sabia, R., Tenerelli, J., Thouvenin-Masson, C., Turiel, A., Vergely, J.L., Vinogradova, N., Wentz, F., Yueh, S., 2020. Sea surface salinity estimates from spaceborne L-band radiometers: an overview of the first decade of observation (2010–2019). Remote Sens. Environ. 242, 111769. ISSN 0034–4257. https://doi.org/10.1016/j.rse.2020.111769.
Rodríguez-Fernández, Anterrieu, et al., 2019. SMOS-HR: a high resolution L-band passive radiometer for earth science and applications. IEEE Symp. Geosci. Remote Sens. 2019, 8392–8395.
Sakov, P., Counillon, F., Bertino, L., Lisæter, K.A., Oke, P.R., Korablev, A., 2012. TOPAZ4: an ocean-sea ice data assimilation system for the North Atlantic and Arctic. Ocean Sci. 8, 633–656. https://doi.org/10.5194/os-8-633-2012.
Shiklomanov, I.A., et al., 1998. World Water Resources. A New Appraisal and Assessment for the 21ST Century. United Nations, Educational, Scientific and Cultural Organization.
Stroh, J.N., Panteleev, G., Kirillov, S., Makhotin, M., Shakhova, N., 2015. Sea-surface temperature and salinity product comparison against external in situ data in the Arctic Ocean. J. Geophys. Res. Oceans 120, 7223–7236. https://doi.org/10.1002/2015JC011005.
Tang, W., Yueh, S., Yang, D., Fore, A., Hayashi, A., Lee, T., Fournier, S., Holt, B., 2018. The potential and challenges of using soil moisture active passive (SMAP) sea surface salinity to monitor Arctic Ocean freshwater changes. Remote Sens. https://doi.org/10.3390/rs10060869.
Tarasenko, A., Supply, A., Kusse-Tiuz, N., Ivanov, V., Makhotin, M., Tournadre, J., Chapron, B., Boutin, J., Kolodziejczyk, N., 2019. Surface Waters Properties in the Laptev and the East-Siberian Seas in Summer 2018 from In Situ and Satellite Data. Ocean Sci. Discuss. https://doi.org/10.5194/os-2019-60. in Review.
Ulaby, F., Moore, R., Fung, A., 1990. Microwave Remote Sensing: Active and Passive. vol. 3 Artech House, Boston, Mass.
Vinogradova, N., Lee, T., Boutin, J., Drushka, K., Fournier, S., Sabia, R., Stammer, D., Bayler, E., Reul, N., Gordon, A., Melnichenko, O., Li, L., Hackert, E., Martin, M., Kolodziejczyk, N., Hasson, A., Brown, S., Misra, S., Lindstrom, E., 2019. Satellite salinity observing system: recent discoveries and the way forward. Front. Mar. Sci. 6, 243. https://doi.org/10.3389/fmars.2019.00243.
Waldteufel, P., Vergely, J.L., Cot, C., 2004. A modified cardioid model for processing multiangular radiometric observations. IEEE Trans. Geosci. Remote Sens. 42, 1059–1063.
Xie, J., Raj, R.P., Bertino, L., Samuelsen, A., Wakamatsu, T., 2019. Evaluation of Arctic Ocean surface salinities from the Soil Moisture and Ocean Salinity (SMOS) mission against a regional reanalysis and in situ data. Ocean Science 15 (5), 1191–1206. https://www.ocean-sci.net/15/1191/2019 https://doi.org/10.5194/os-15-1191-2019.
Yueh, S.H., West, R., Wilson, W.J., Li, F.K., Njoku, E.G., Rahmat- Samii, Y., 2001. Error sources and feasibility for microwave remote sensing of ocean surface salinity. IEEE Trans. Geosci. Remote Sens. 39 (5), 1049–1060.